

POLITECNICO DI TORINO

Department of Mechanical and Aerospace Engineering

Master degree course in Aerospace Engineering

Master Degree Thesis

Analysis of Multistage Structures using Cyclic Symmetry



Avio Aero 
A GE Aviation Business

Supervisors

Prof. Christian Maria Firrone
Ing. Antonio Giuseppe D'Ettole
Ing. Marco Moletta

Candidate

Valerio PISCOPO
Student number: 275751

ACADEMIC YEAR 2021-2022

Be greater than average

Abstract

In the last decades, the Aeronautical industry had to face with important challenges towards improving sustainability and reducing environmental impact on climate changes. In this overview, great emphasis is placed on producing engines more efficient and with excellent performance and reliability. These improvements also come from new and innovative analysis techniques applied to the key engine's components; among them, Low Pressure Turbine (LPT) which plays a crucial role.

This thesis deals with the modal and forced response analysis (in which synchronous of engine order type excitations are considered) of a multi-stage assembly of cyclic structures such as, for example, turbine engine bladed disks. Such assemblies are traditionally modeled stage by stage but, in this way, the inter-stage coupling effect can sometime be erroneously neglected. As an answer to this issue, a new method which combines a cyclic modeling of each stage with a realistic inter-stage coupling is here proposed. Study cases and confronts with single stage models and 360 full models are presented in order to evaluate the efficiency of the method first on a simple case study and, then, on a more realistic industrial example.

Acknowledgements

Questo elaborato di tesi è il coronamento di un percorso durato quasi tre anni, in cui ho avuto il costante sostegno di molte persone che, a tal proposito, desidero ringraziare. In primis la mia famiglia, senza i loro sacrifici ed il loro supporto non avrei mai raggiunto questo traguardo: lo dedico a mia sorella e a mio fratello, a mio padre che mi ha insegnato il sacrificio e a mia madre che mi ha trasmesso il senso del dovere.

Un ringraziamento va al Prof. Christian Maria Firrone che ha permesso di concludere il mio percorso di studi con questa esperienza formativa sotto la supervisione degli ingegneri Antonio Giuseppe D'Ettola e Marco Moletta. Grazie per il vostro costante supporto e per l'aver creduto in me.

Non posso che ringraziare i miei conquilini, attuali e passati. EDISU mi ha offerto un tetto e mi ha permesso di incontrarvi, voi lo avete reso una casa e siete diventati la mia famiglia torinese. Questi anni a Torino sono stati fantastici soprattutto grazie a voi.

Ai miei colleghi di corso va la mia gratitudine per l'essere stati presenti fin dal mio primo giorno nella città della Mole. Sebbene la pandemia ci abbia tolto molte delle nostre esperienze, condividere con voi le gioie e le ansie di questo percorso di studi è stato il supporto di cui non avrei saputo fare a meno.

Allo stesso modo, nonostante la distanza, vicini mi sono stati i miei amici di Formia. Le speranze e le aspettative che avete riposto in me mi hanno motivato a dare sempre il massimo guardando con lungimiranza ogni traguardo raggiunto. Grazie per esserci sempre stati.

Gioia, tu mi sei stata vicino dal giorno uno, anche quando le nostre strade si sono divise. Nel corso della mia vita ho imparato molte cose ma non a fare a meno di te. Per l'uomo che sono diventato, per l'ingegnere che diventerò, non posso che ringraziarti perché sarà sempre anche merito tuo.

Per ultimi, non per importanza, ringrazio gli amici di JEToP. Voi mi avete permesso di sviluppare le mie passioni arricchendo il mio percorso accademico. Vi auguro ogni successo umano e professionale.

Contents

List of Figures	IV
List of Tables	VII
1 Introduction	1
1.1 The GREAT 2020	1
1.2 The aircraft engines	2
1.2.1 Turbojet	5
1.2.2 Turbofan	5
1.2.3 Turboprop	6
1.2.4 Turboshaft	6
1.3 Low Pressure Turbine - LPT	7
2 Rotor Dynamics	9
2.1 Cyclic symmetry	9
2.2 Modal Analysis	14
2.3 Reduction techniques	22
2.3.1 Modal reduction	22
3 Aeromechanical instabilities	24
3.1 Aerodynamic of turbines	25
3.2 Aeroelasticity in turbomachines	27
3.2.1 Flutter	27
4 Forced Response	34
4.1 Static and Dynamics loads	34
5 Dynamical Analysis of Multistage Cyclic Structures	38
5.1 Multistage Cyclic Symmetry method	38

5.2	Multistage Cyclic Symmetry application	41
5.3	Modal Assurance Criterion (MAC)	44
5.3.1	MAC calculation	45
5.4	Results	46
5.4.1	Test case A	46
5.4.2	Test case B	53
6	Forced Response of Multistage Cyclic Structures	57
6.1	Results	58
6.1.1	Test case A	58
6.1.2	Test case B	60
7	Conclusions and future developments	62
	Bibliography	63

List of Figures

1.1	ACARE objectives [12].	2
1.2	Thermodynamic cycle of jet engine [7].	3
1.3	Aircraft engine [1].	4
1.4	Turbojet engine [26].	5
1.5	Turbojet engine sketch.	5
1.6	Turbofan engine [25].	5
1.7	Turbofan engine sketch.	5
1.8	Turboprop engine [27].	6
1.9	Turboshaft engine[28].	6
1.10	Turbine sketch with highlighted stage.	7
2.1	Example of cyclic symmetry structure.	10
2.2	Cyclic symmetry structure with two nodal diameters.	12
2.3	Stationary mode.	14
2.4	Stationary anti-phase mode.	15
2.5	Rotating mode.	15
2.6	Time evolution of eigenvector u_i	17
2.7	Time evolution of rotating eigenvector.	17
2.8	Sector of a cyclic symmetry structure.	17
2.9	FEM sectors modelling [4].	18
2.10	Blade mode shapes.	20
2.11	Example of FreND diagram.	20
2.12	Veering region example [8].	21
3.1	Collar's triangle.	24
3.2	Example of wake [29].	27
3.3	Example of a 2 DOF system.	28
3.4	Unstable system response.	29
3.5	Obscillatory system response.	29
3.6	Stable system response.	30

3.7	Aerodynamic coupling on a blade row.	30
3.8	Aerodynamic coupling as function of IBPA.	32
3.9	Example of aeroplots.	33
4.1	Example of a Campbell diagram [16].	36
4.2	Zig-zag diagram.	36
4.3	Aliasing.	37
5.1	Turbomachinery Multistage Cyclic Structure [18].	39
5.2	Gear (A) modeled as a Multistage Cyclic Structure with two stages (B) [18].	39
5.3	Finite element model of 2 cyclic structures with 24 and 45 sectors [14]. . .	41
5.4	Example of a sector from a rotating stage.	42
5.5	Example of a sector from a rotating stage with a drilled part.	42
5.6	Nodes whose displacements along z-axis and y-axis are forbidden.	43
5.7	Modal shape, Harmonic Index equal to 0 , Frequency = 617.8 Hz , Dis- placements in [mm] - back and front view -.	44
5.8	3D MAC plot example.	45
5.9	Sector from stage 1 (green color) and sector from stage 2 (orange color). .	46
5.10	360 full model with two stages of 8 and 11 sectors.	47
5.11	Modal shape of 360 full model, Frequency = 71 Hz.	47
5.12	nodes selected due to extract Harmonic Index from 360 full model.	48
5.13	Displacements of node selected in Figure 5.12, Fr = 71 Hz.	48
5.14	Modal shape, Harmonic Index equal to 2 , 360 Model Frequency = 71 Hz (left figure), Multistage Model Frequency = 75 Hz (right figure).	49
5.15	Modal shape, Harmonic Index equal to 3 , 360 Model Frequency = 157 Hz (left figure), Multistage Model Frequency = 157 Hz (right figure).	49
5.16	Modal shape, Harmonic Index equal to 4 , 360 Model Frequency = 198 Hz (left figure), Multistage Model Frequency = 197 Hz (right figure).	49
5.17	Modal shape, Harmonic Index equal to 4 , 360 Model Frequency = 220 Hz (left figure), Multistage Model Frequency = 220 Hz (right figure).	50
5.18	Modal shape, Harmonic Index equal to 0 , 360 Model Frequency = 228 Hz (left figure), Multistage Model Frequency = 239 Hz (right figure).	50
5.19	Modal shape, Harmonic Index equal to 3 , 360 Model Frequency = 240 Hz (left figure), Multistage Model Frequency = 241 Hz (right figure).	50
5.20	Modal shape, Harmonic Index equal to 4 , 360 Model Frequency = 306 Hz (left figure), Multistage Model Frequency = 305 Hz (right figure).	51
5.21	Modal shape, Harmonic Index equal to 1 , 360 Model Frequency = 340 Hz (left figure), Multistage Model Frequency = 340 Hz (right figure).	51

5.22	Modal shape, Harmonic Index equal to 4 , 360 Model Frequency = 461 Hz (left figure), Multistage Model Frequency = 459 Hz (right figure).	51
5.23	MAC calculation: Multistage VS 360 full model (case A).	52
5.24	Sector from stage 1 (blue color) and sector from stage 2 (green color). Left figure shows isometric view; right one top view.	53
5.25	360 full model with two stages of 48 and 54 sectors (mesh has been hided due to obtain a clearer visualization).	53
5.26	Modal shape, Harmonic Index equal to 3 , 360 Model Frequency = 1529 Hz (left figure), Multistage Model Frequency = 1507 Hz (right figure). . .	54
5.27	Modal shape, Harmonic Index equal to 1 , 360 Model Frequency = 1521 Hz (left figure), Multistage Model Frequency = 1525 Hz (right figure). . .	54
5.28	Modal shape, Harmonic Index equal to 0 , 360 Model Frequency = 1620 Hz (left figure), Multistage Model Frequency = 1620 Hz (right figure). . .	54
5.29	Modal shape, Harmonic Index equal to 4 , 360 Model Frequency = 1637 Hz (left figure), Multistage Model Frequency = 1634 Hz (right figure). . .	55
5.30	Modal shape, Harmonic Index equal to 1 , 360 Model Frequency = 2571 Hz (left figure), Multistage Model Frequency = 2562 Hz (right figure). . .	55
5.31	Modal shape, Harmonic Index equal to 5 , 360 Model Frequency = 4114 Hz (left figure), Multistage Model Frequency = 4109 Hz (right figure). . .	55
5.32	MAC calculation: Multistage VS 360 full model (case B).	56
6.1	360 Full Model (left) vs Multistage (center) vs Single Stage (right) - Mode 1 - Harmonic Index = 2.	58
6.2	Excitation applied on the upper stage. Good matching in terms of Frequency Response in case no coupling effect is shown.	58
6.3	360 Full Model (left) vs Multistage (center) vs Single Stage (right) - Mode 4 - Harmonic Index = 4.	59
6.4	Excitation applied on the upper stage. Not good matching in terms of Frequency Response in case coupling effect is significant.	59
6.5	360 Full Model (left) vs Multistage (center) vs Single Lower Stage (right) - Mode 10 - Harmonic Index = 4.	60
6.6	Excitation applied on the lower stage. Good matching in terms of Frequency Response in case no coupling effect is shown.	60
6.7	360 Full Model (left) vs Multistage (center) vs Single Lower Stage (right) - Mode 4 - Harmonic Index = 2.	61
6.8	Excitation applied on the lower stage. Not good matching in terms of Frequency Response in case coupling effect is significant.	61

List of Tables

5.1	Modal Analysis confront between Multistage and 360 full model (case A).	52
5.2	Modal Analysis confront between Multistage and 360 full model (case B).	56

Chapter 1

Introduction

1.1 The GREAT 2020

The GREAT 2020 (GReen Engine for Air Traffic), is a research project started in 2009 financed by Regione Piemonte in which, the European Commission, together with experts group ACARE (Advisory Council for Aviation Research and Innovation in Europe), set a list of strategic goals to be reached by the aeronautical sector within 2020 and 2050 in terms of environmental impact and efficiency. These goals can be summarized in the following points:

- higher efficiency related to an overall quality improvement of the service offered to the user, including safety, vehicle on-board comfort and flight punctuality;
- a drastic reduction of the environmental impact.

The above-mentioned purposes bring into play every level of the aeronautic and research sector. So that, this thesis work is part of a project in which several companies are involved:

- **AvioAero:** a GE Aviation business, leader in the design, maintenance and manufacturing of aeronautical components, which constitutes a center of competence for the entire General Electric group regarding mechanical transmissions and low-pressure turbines design, suited in Turin, Pomigliano D'Arco and Poland.
- **Politecnico di Torino:** one of the most prestigious public organizations worldwide for its formation and research activities in engineering and architecture. A prime actor of the project is the Greatlab, a shared working area born in 2008 from the partnership between Politecnico di Torino and AvioAero.

- **ISTEC-CNR:** The Turin detail of the Istituto di Scienza e Tecnologia dei materiali Ceramici which as part of the GREAT2020 carries out research on environmentally-friendly processing systems of aeronautical alloys.
- **La Regione Piemonte:** host of the project and ideal soil for the development and the growth of the GREAT 2020, who has always been committed to the promotion of industrial competitiveness, resulting in an active support for the GREAT2020 project.

Those ambitious goals, regarding a reduction of 50% of CO₂ emissions, of 80% of NO_x one and a reduction of 18dB about the perceived noise can be reached by a strong collaboration among cited companies and an huge research in new technologies. The quantity of CO₂ produced is proportional to the fuel burned, therefore, a reduction in the emission could be reached increasing the total efficiency of the engine or decreasing the weight of the components of the engine. This means to develop lighter and more resistant blades, more performing combustors and thus new manufacturing processes allowing to handle innovative materials.

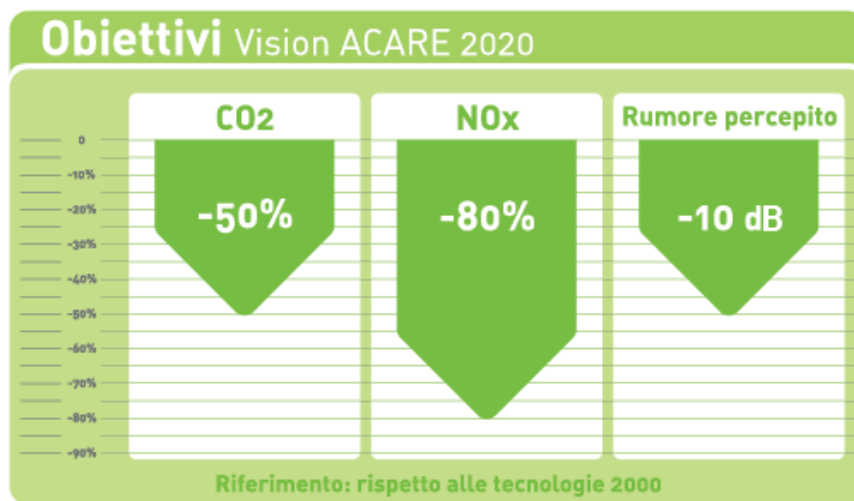


Figure 1.1: ACARE objectives [12].

1.2 The aircraft engines

In the history of aviation several solutions are proposed as propulsion system for aircrafts [22]. The first attempts of using gas turbine engines as aircraft power plants date back to 1913 when René Lorin, a French engineer, patented the first jet propulsion engine that,

due to undeveloped suitable heat resisting materials and inefficiency at low speeds, could not be manufactured or used at that time. Later, in 1930, Frank Whittle obtained his first patent for using a gas turbine to produce a propulsive jet. Even though it completed its first flight only eleven years later, it can be said that Whittle's engine set the basis for the modern gas turbine. In this chapter only a general overview of the most important ones is described.

Jet propulsion is a practical application of Newton's Third Law that states: "*for every force acting on a body, there is an opposite and equal reaction*". In this case, the engines take the atmospheric air, energize it (accelerating it), and the resultant of this force applied to the air, is a reaction to the engine in the opposite direction. Since the engine is linked rigidly to an aircraft, the same force is transmitted to the last one. This reaction force, called *thrust*, is proportional to the variation of velocity and to the mass flow rate of air managed by the engine. Thus, the same thrust can be obtained by giving a small acceleration to a large mass of air or by giving a large acceleration to a small quantity of air. In practice, the former option is preferred in order to maximize the efficiency: the higher is the velocity, the higher can be the losses.

The engine working cycle is the *Bryaton's cycle* represented in Figure 1.2 and composed by four phases: induction, compression, combustion and exhaust.

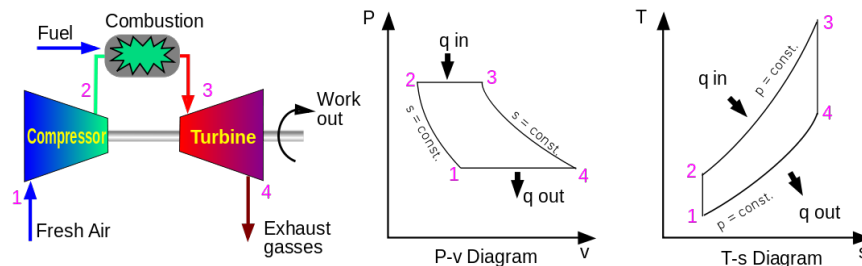


Figure 1.2: Thermodynamic cycle of jet engine [7].

As shown in the Figure 1.3, each engine is made by those components:

- **Air intake:** the channeling part in which the air enter to the engine system;
- **Compressor:** often divided in Low Pressure Compressor (LPC) and High Pressure Compressor (HPC) and it is aimed to compress air mass flow rate;
- **Combustor:** in which part of the air is mixed with the fuel with a stoichiometric ratio around 50:1 and it is burnt;

- **Turbine:** as the compressor, it is often divided in Low Pressure Turbine (LPC) and High Pressure Turbine (HPT) and it expands the exhaust gas;
- **Exhaust system:** accelerates the exhaust gasses in order to get the thrust.

Compressor and turbine are divided in Low and High parts in order to decoupling rotational velocity. This partition reduce the mass flow rate of air to elaborate in order to produce the same thrust resulting in an aerodynamic efficiency improvement.

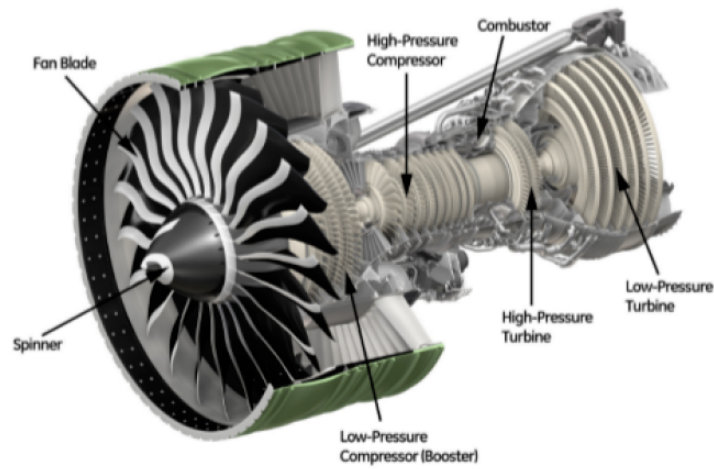


Figure 1.3: Aircraft engine [1].

1.2.1 Turbojet

Even if turbojet engine model is outdated, it can be considered as the starting reference point of the other engines (turbofan, turboprop and turboshaft). Observing the Figure 1.4, after entering the engine through an inlet duct, the air is channeled entirely in the compressor that increases its pressure and then reach the combustion chamber, where fuel is injected. The heat developed by the combustion leads to an expansion into the turbine. The turbine exhaust is then expanded in the nozzle, where it is accelerated to high speed to provide thrust.

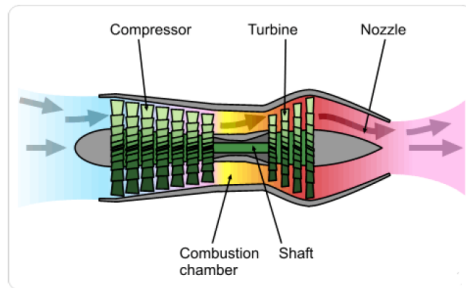


Figure 1.4: Turbojet engine [26].

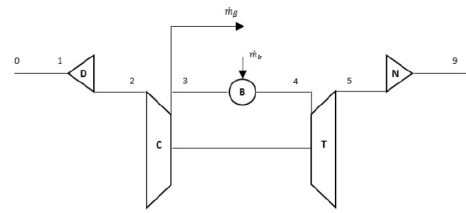


Figure 1.5: Turbojet engine sketch.

1.2.2 Turbofan

Starting from the turbojet model, the turbofan engine is characterized by a fan before the compressor stages, Figure 1.6. In this case, the quantity of air processed is bigger than the previous one but not all the air goes in the combustor. An important parameter is the *bypass ratio* defined as the ratio between the air elaborated in the combustor and the total air processed. In modern engines ratios from 4:1 to 8:1 are employed. This configuration allows to produce the same thrust of the turbojet engine, with a low velocity variation, this means lower losses and thus higher efficiencies.

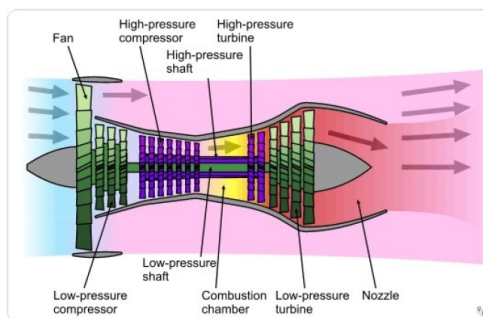


Figure 1.6: Turbofan engine [25].

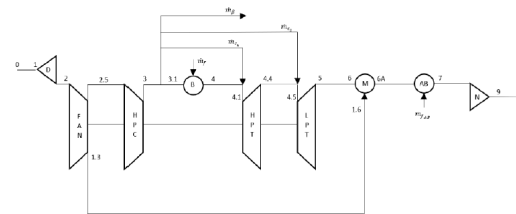


Figure 1.7: Turbofan engine sketch.

1.2.3 Turboprop

In the turboprop engine (jet engine derivatives) a portion of the engine's thrust is produced by spinning a propeller and the remaining part comes from the high-speed jet exhaust. Instead of turbofans, where the fan only contributes to a minor part of the thrust production, in turboprop the propeller usually provides the majority of thrust. As can be seen in Figure 1.8, most turboprops use gear reduction between the turbine shaft and the propeller. These engine have better performance than turbojets or turbofans at low speeds (where propeller efficiency is high), while they tend to become noisy and inefficient at high speeds due to turbulence and sonic conditions.

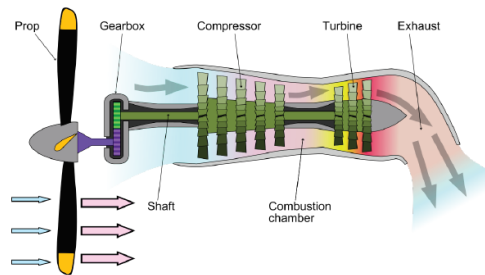


Figure 1.8: Turboprop engine [27].

1.2.4 Turboshaft

The turboshaft engine is similar to the turbojet engine with a post expansion after turbine stages, Figure 1.9, in which the fluid is much more accelerated producing a much higher thrust. This type of engine is used in case of high power output, small size and weight and high reliability.

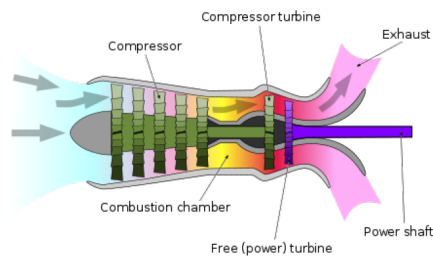


Figure 1.9: Turboshaft engine[28].

1.3 Low Pressure Turbine - LPT

As highlighted before, the turbine has the task of providing the power to drive the compressor and the shaft power to the propeller or rotor when they are present. High compression ratio engines usually feature two shafts, so two turbines: the high-pressure turbine drives the high-pressure compressor, while the low-pressure turbine drives the low-pressure compressor and, for turbofan engines, the fan. In this section components belonging to a LPT and their main features are described. Turbines are classified depending on gas-flow direction:

- *axial*: the fluid moves parallelly to the rotation axis;
- *radial*: the fluid moves radially to the rotational axis.

Moreover, turbines can be divided in stages which is the fundamental operating macro-group that exploits energy from the fluid, Figure 1.5.

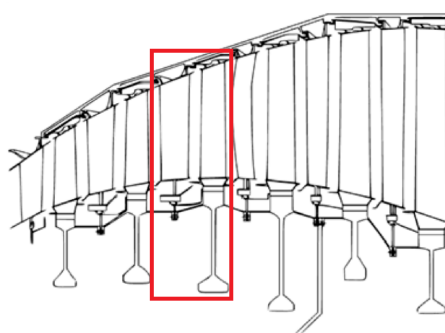


Figure 1.10: Turbine sketch with highlighted stage.

The single stage of a turbine is made by two groups:

- ***Stator***: it is the fixed part of a turbine and it is composed by statoric blades which prepare the fluid to be exploitable from rotor imposing a velocity direction and by case which is the structure.
- ***Rotor***: it is the rotating part composed by rotoric blades linked to the rotating disk, which is jointed to the main shaft.

The turbines' design process requires the best compromise between efficiency and reliability. In this purpose, several parameters must be considered:

- *Mechanical power*: it is the power which is possible to extract from the engine. Under 1D hypothesis it is equal to $\dot{m}(u_1c_{1u} - u_2c_{2u})$ where \dot{m} is the mass flow rate of processed fluid, u is the blade peripheral speed and c_u is the fluid velocity projected along u while $(1,2)$ stand for inlet and outlet respectively.
- *Degree of reaction*: it is the ratio between the enthalpy extracted in the rotor and the energy extracted in the stage:

$$R = \frac{\Delta H_{rotor}}{\Delta H_{total}} = \frac{h_2 - h_1}{h_{01} - h_{02}}. \quad (1.1)$$

It is a measure of the allocation of expansion made in the stator and in the rotor. Typical values are:

- $R = 0$ for an *impulse turbine* in which expansion is totally made in the stator;
- $R = 0.5$ which defines a *reaction turbine* where expansion is split equally in the rotor and in the stator. Under isotropic condition, in this case airfoil shape generates counter symmetric velocity triangles.

Centrifugal forces cause a changing in degree of reaction along the radial coordinate of high blades: *twiset-blades*.

- *Thermo-structural parameters* like mechanical strength, High Cycle Fatigue (HCF), Low Cycle Fatigue (LCF) and Creep.

The first two are related with aerodynamic aspects which affects the efficiency, while the latter with dynamic one which affects reliability. As explained before, higher power means higher mass flow rates (to keep the velocity lower because of efficiency), which leads to an higher quantity of fluid to deflects and so higher loads. This bring to a reduction of the blade life (and reliability).

Summarizing, the rotor components are:

- *Airfoil*: it is the operative component in which the fluid flows and produce work.
- *Shroud*: it is at the blade tip and provide many functions: ensure tightness, increase blade stiffness, enhance damping contribution.
- *Shank*: it is the linkage between airfoil and the part anchored to the disk.
- *Dovetail*: it is the linking part between blade and disk and can have several shapes (also fir tree).

Chapter 2

Rotor Dynamics

In order to optimize the design of bladed disks, all the sources of stresses have to be taken into account. Among these, a particular importance is usually given to the time-varying excitation, as they are the major responsible of failure due to HCF (High Cycle Fatigue). Therefore, studying the bladed discs dynamics is essential in order to obtain an accurate prediction of natural frequencies and mode shapes and avoid resonances and instabilities.

2.1 Cyclic symmetry

Bladed disks fall in the category of structures showing *cyclic symmetry*, which means that they consist of a finite number of identical substructures or sectors forming a closed geometry. In case of LPT the cyclic symmetry is characterized by identical sectors defined by the sector angle $\alpha = \frac{2\pi}{N}$, the so-called *sector angle* where N is the number of sectors, which is, for LPTs, the number of blades.

Discretizing the bladed disk in Finite Elements [5], it is possible to obtain the equation of motion:

$$[M]\{\ddot{x}\} + [K]\{x\} = \{F\} \quad (2.1)$$

where $\{x\}$ is the position vector relative to degrees of freedom of Finite Element nodes, while $[M]$ and $[K]$ are respectively the *mass* and the *stiffness* matrices and $\{F\}$ is the vector of the external forces. These vectors have the following dimension: $\{x\}$ is $3n_n \times 1$ as well as $\{F\}$, while $[M]$ and $[K]$ are square matrices of dimension $3n_n \times 3n_n$ where n_n is the number of nodes of the entire system.



Figure 2.1: Example of cyclic symmetry structure.

Usually, assuming z - axis as the rotating one for a cyclic symmetry structure, the node vector $\{x\}$ is rewritten in cylindrical coordinate applying the transformation:

$$\begin{aligned} x &= \rho \cos \theta \\ y &= \rho \sin \theta \end{aligned} \tag{2.2}$$

Moreover, considering the cyclic symmetry properties, the vector $\{x\}$ can be decomposed in a sub-set of nodal vectors for each sector, as well as the force vector, obtaining:

$$\{x\} = \begin{Bmatrix} \{x_1\} \\ \{x_2\} \\ \{x_3\} \\ \vdots \\ \{x_{N-1}\} \\ \{x_N\} \end{Bmatrix} \quad \{F\} = \begin{Bmatrix} \{F_1\} \\ \{F_2\} \\ \{F_3\} \\ \vdots \\ \{F_{N-1}\} \\ \{F_N\} \end{Bmatrix} \tag{2.3}$$

where $\{x_i\}$ represents the nodal coordinate of the sector i_{th} for $i = 1, \dots, N$.

These steps allow the following re-arranging for the mass and stiffness matrices:

$$[M] = \begin{bmatrix} M_0 & M_1 & M_2 & \cdots & M_2 & M_1 \\ M_1 & M_0 & M_1 & \cdots & M_3 & M_2 \\ M_2 & M_1 & M_0 & \cdots & M_4 & M_3 \\ \vdots & \vdots & \vdots & \ddots & \vdots & \vdots \\ M_2 & M_3 & M_4 & \cdots & M_0 & M_1 \\ M_1 & M_2 & M_3 & \cdots & M_1 & M_0 \end{bmatrix} \quad (2.4)$$

$$[K] = \begin{bmatrix} K_0 & K_1 & K_2 & \cdots & K_2 & K_1 \\ K_1 & K_0 & K_1 & \cdots & K_3 & K_2 \\ K_2 & K_1 & K_0 & \cdots & K_4 & K_3 \\ \vdots & \vdots & \vdots & \ddots & \vdots & \vdots \\ K_2 & K_3 & K_4 & \cdots & K_0 & K_1 \\ K_1 & K_2 & K_3 & \cdots & K_1 & K_0 \end{bmatrix} \quad (2.5)$$

Where the sub-matrices $[M_n]$ and $[K_n]$ ($n = 0, \dots, \text{floor}(N/2)$ if N is even or $n = 0, \dots, \text{floor}((N-1)/2)$ if N is odd) are symmetric as well as $[M]$ and $[K]$ that have a *block circulant symmetric* structure. Defining n_s the number of DOF belonging to a sector, the dimension of $[M_n]$ and $[K_n]$ is $n_s \times n_s$.

A single sector can be divided in three different parts:

- left-hand side nodes defined as those nodes at left interface between 2 consecutive sectors;
- right-hand side nodes defined as those nodes at right interface between 2 consecutive sectors;
- inner nodes which are the not above-mentioned nodes.

In this way the displacement vector $\{x_j\}$ and the force vector $\{F_j\}$ can be rewritten as:

$$\{x^s\} = \begin{Bmatrix} \{x_R^s\} \\ \{x_L^s\} \\ \{x_I^s\} \end{Bmatrix} \quad (2.6)$$

$$\{F^s\} = \begin{Bmatrix} \{F_R\} \\ \{F_L\} \\ \{F_I\} \end{Bmatrix} \quad (2.7)$$

Another important parameter for a cyclic symmetry structure is the *Inter Blade Phase Angle* (IBPA), defined as the ratio between the number of nodal diameters and the number of blades. In a cyclic symmetric structure, a nodal diameter is the place of aligned points passing through the center of rotation characterized by null nodal displacements (see Figure 2.2).

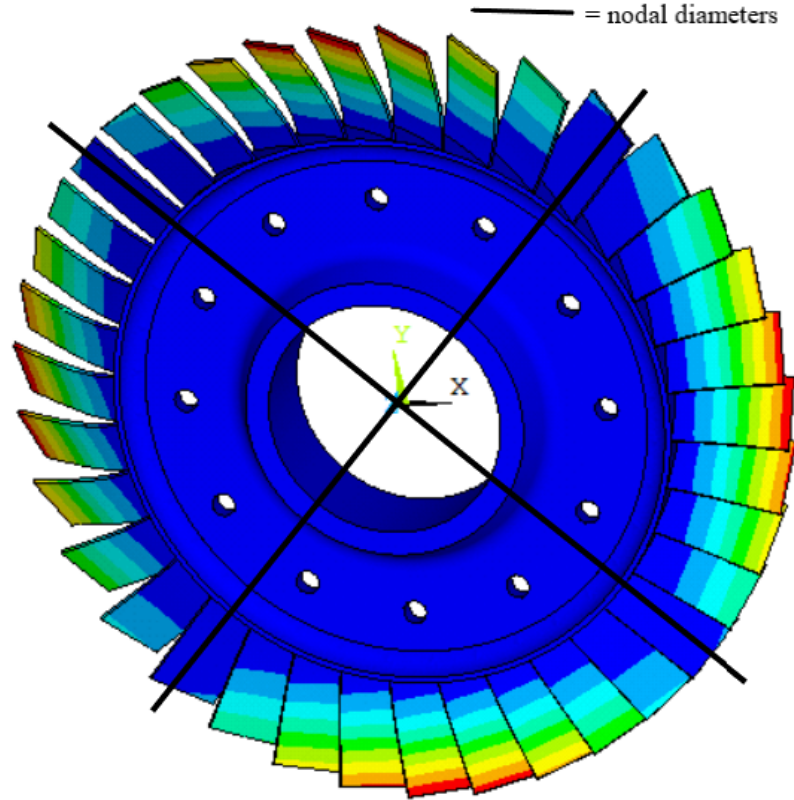


Figure 2.2: Cyclic symmetry structure with two nodal diameters.

IBPA can be defined as:

$$\varphi_n = \frac{2\pi n}{N} \quad (2.8)$$

where n is the nodal diameter and N is the number of sectors. In a cyclic symmetric structure, the nodal diameters and so IBPA assume values included in these ranges:

$$\begin{cases} 0 \leq n \leq \frac{N}{2} & \text{if } N \text{ is even} \\ 0 \leq n \leq \frac{N-1}{2} & \text{if } N \text{ is odd} \end{cases} \quad (2.9)$$

Thus, with IBPA, it is possible to link Left and Right interfaces according to:

$$\{x_R^s\} = \{x_L^s\}e^{i\varphi_n}, \quad (2.10)$$

and so:

$$\{x^s\} = \begin{Bmatrix} \{x_L^s \cdot e^{i\varphi_n}\} \\ \{x_L^s\} \\ \{x_I^s\} \end{Bmatrix}. \quad (2.11)$$

Remembering the Euler's Identity ($e^{i\varphi_n} = \cos\left(\frac{2\pi n}{N}\right) + i\left(\frac{2\pi n}{N}\right)$), it can be easily understood that the first row of the previous vector has imaginary part equal to 0 for $n = 0$ and $n = N/2$. This means that, for those values, the eigen problem returns only real displacements.

Moreover, with the IBPA it is possible to link displacements and forces between sectors allowing to reduce the system analysis to the single sector. This reduction is provided by the fact that the *Left-side* for a sector is the *Right-side* of the adjacent one,. Thus, defining a force vector to a sector as $F^s = F_0^s e^{i\omega t}$ the stationary solution can be written as:

$$([K^s] - \omega^2[M^s])\{x^s\} = F_0^s \quad (2.12)$$

and the solution can be expanded cyclically by the IBPA obtaining overall solution.

2.2 Modal Analysis

Modal analysis is the study of the free vibration of a dynamic system. After the mass and the stiffness matrix are obtained through the FE model, natural frequencies and mode shapes can be extracted solving the following eigenproblem:

$$([K] - \omega_i^2[M])\{u_i\} = 0 \quad (2.13)$$

where $[K]$ and $[M]$ are the block circulant matrices defined in (2.4) and (2.5) while ω_i and $\{u_i\}$ are respectively the i -th eigenvalue and eigenvector.

When looking at the mode shapes of a cylindrical symmetrical structure, there three possible cases [21]:

- **Stationary modes:** each sector has the same mode shape as its neighbors and vibrates in-phase with them:

$$\{u_{n_i}\} = \{u_{n+1_i}\} \quad \forall n \quad (2.14)$$

As it is shown in Figure 2.3, a rotation of the mode shape of an arbitrary number of sectors would leave the mode shape unchanged. In this case what we observe is a *standing wave mode shape*, which is described by a single eigenvalue and a single eigenvector. This mode is obtained when $\varphi_n = 0$ and so, recalling equation (2.8), when the number of nodal diameter is equal to 0.

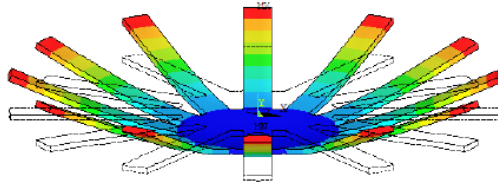


Figure 2.3: Stationary mode.

- **Stationary anti-phase modes:** each sector has the same mode shape as its neighbors, but it vibrates in anti-phase with them, Figure 2.4:

$$\{u_{n_i}\} = -\{u_{n+1_i}\} \quad \forall n \quad (2.15)$$

This mode is obtained when $\varphi_n = \pm\pi$ and it is valid only if N is even. In this case, a rotation of the mode shape of an even number of sectors leaves the mode shape unchanged, while a rotation of an odd number of sections will result in a

mode shape with inverted sign. However, it is still a standing mode and so it can be described by a single eigenvalue and a single eigenvector.

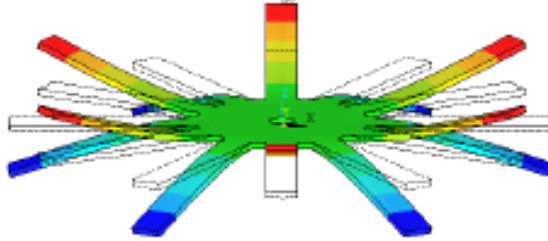


Figure 2.4: Stationary anti-phase mode.

- **Rotating modes:** the sector moves with different phases, Figure 2.5, and so:

$$\{u_{n_i}\} \neq \pm\{u_{n+1_i}\} \quad \forall n \quad (2.16)$$

This mode is obtained for all the other values of φ_n .

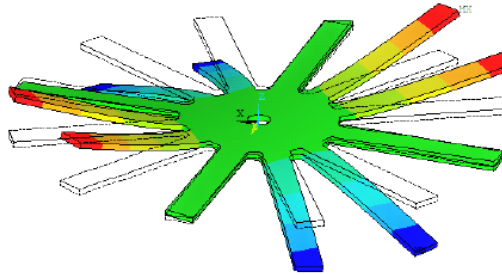


Figure 2.5: Rotating mode.

These last modes occur in orthogonal pairs of standing waves, described by the same eigenvalue and the same eigenvector. Their combination results in a *rotating mode shape*. Since all the sectors are identical, by shifting a mode shape $\{u_i\}$ of one sector's angle α_n , the new mode shape $\{u'_i\}$ will have the same eigenvalue as the starting mode shape. In other words it is possible to define, for a given eigenvalue, a couple of eigenvectors such as:

$$\{u_i\} \cdot \{\bar{u}_i\} = 0 \quad (2.17)$$

and so the new mode can be defined as:

$$\{u'_i\} = c\{u_i\} + s\{\bar{u}_i\} \quad (2.18)$$

where, assuming normalized eigenvectors c and s coefficient can be written as:

$$\begin{aligned} c &= \cos \varphi_n \\ s &= \sin \varphi_n \end{aligned} \quad (2.19)$$

Repeating the same passages to the eigenvector $\{\bar{u}_i\}$ applying the sector angle shift, it is possible to obtain an other eigenvector $\{\bar{u}_i'\}$ which is orthogonal to $\{u_i'\}$ and equal to:

$$\{\bar{u}_i'\} = -s\{u_i\} + c\{\bar{u}_i\} \quad (2.20)$$

Thus:

$$\begin{Bmatrix} u_i' \\ \bar{u}_i' \end{Bmatrix} = \begin{bmatrix} cI_{Nn_s} & sI_{Nn_s} \\ -sI_{Nn_s} & cI_{Nn_s} \end{bmatrix} \begin{Bmatrix} u_i \\ \bar{u}_i \end{Bmatrix} = R \begin{Bmatrix} u_i \\ \bar{u}_i \end{Bmatrix} \quad (2.21)$$

This results allows to represent the modeshape of consecutive sectors, in fact:

$$\begin{Bmatrix} u_{(n-1)1} \\ \bar{u}_{(n-1)1} \end{Bmatrix} = R \begin{Bmatrix} u_{n_i} \\ \bar{u}_{n_i} \end{Bmatrix} \quad \forall n \quad (2.22)$$

Moreover, if u_i' and \bar{u}_i' are the solutions for the equation (2.13), also a linear combination of both is again a solution like:

$$\begin{aligned} z_i &= u_i + j\bar{u}_i \\ \bar{z}_i &= u_i - j\bar{u}_i \end{aligned} \quad (2.23)$$

which are solutions of the eigenproblem. Thus, under a physical point of view, mode shape of stationary evolution is graphically shown in Figure 2.6 and expressed by the following equation:

$$\text{Re}(\{u_i\}e^{j\omega t}) = \{u_i\} \cos(\omega t) \quad (2.24)$$

In general, it is possible to have real and complex eigenvectors that differ in that for real ones all the DOFs pulsate without any relative delay between them, while for complex eigenvectors the same instantaneous spatial configuration appears rotated of one sector after an interval of time $t = \varphi_h/\omega$ as shown in Figure 2.7. So that, in case of complex eigenvectors the mode shape is:

$$\text{Re}(\{z_i\}e^{j\omega t}) = \{u_i\} \cos(\omega t) - \{\bar{u}_i\} \sin(\omega t) \quad (2.25)$$

in which, for $t = 0 \rightarrow \text{Re}(\{z_i\}e^{j\omega t}) = \text{Re}(\{u_i\}e^{j\omega t})$, while for $t = \varphi_n/\omega \rightarrow \text{Re}(\{z_i\}e^{j\omega t}) = \text{Re}(\{u_i'\}e^{j\omega t})$.

This result can be explained considering that the complex eigenvector contains both

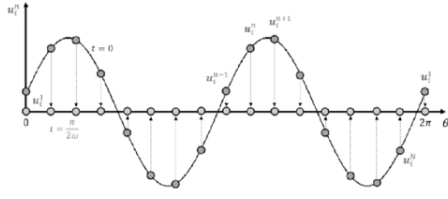


Figure 2.6: Time evolution of eigenvector u_i .

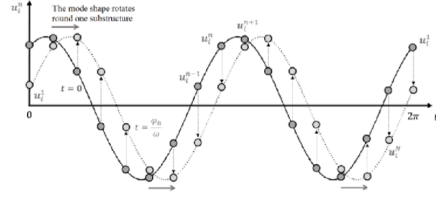


Figure 2.7: Time evolution of rotating eigenvector.

modes ($\{u_i\}, \{\bar{u}_i\}$) and so, for a given sector at a specific time t_0 , shows the same amplitude of the consecutive sector at time $t_0 + \varphi_n/\omega$. Moreover, if the complex eigenvector $\{z_i\}$ presents a clockwise motion, the eigenvector $\{\bar{z}_i\}$ shows a counter-clockwise motion and finally the relation which links the deformed shape between 2 consecutive sectors is:

$$\{z_{(n-1)_i}\} = \{z_{n_i}\}e^{j\varphi_n} \quad (2.26)$$

Generally speaking, for a bladed disk we are more interested in complex modes rather than the real modes since the latter can then be interpreted as the sum of the two counter rotating traveling waves. Note that, if we want to investigate the mode shapes belonging to a the whole bladed disk, in addition to the rising of computational costs and processing time, we could only find real modes since FEM solvers resolve the eigenproblem 2.13 in the real domain.

As highlighted before, due to cyclic symmetry properties, performing a modal analysis of the single sector (Figure 2.8) allows to extend this analysis to the entire bladed disk without prohibitive computational costs.

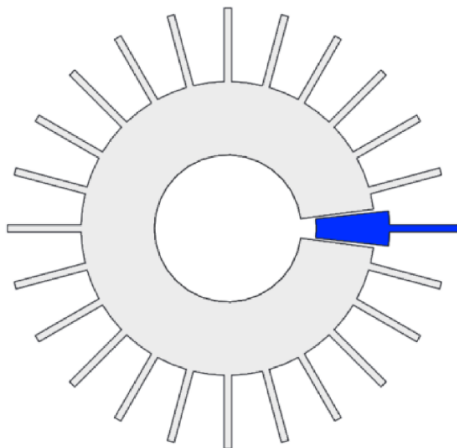


Figure 2.8: Sector of a cyclic symmetry structure.

At this point, several ways to perform modal analysis [4] can be presented. Among these, that one proposed by D.J. Mead according to which it is possible to express (referring also to Figure 2.9) the vector containing the sector DOFs as follows:

$$\{x_s\} = \begin{Bmatrix} x_l \\ x_i \\ x_r \end{Bmatrix} \quad (2.27)$$

where x_l represents the DOFs at the left frontier of the fundamental sector; x_i represents the internal DOFs of the fundamental sector, i.e. those not shared with the neighbor sectors; x_r represents the DOFs at the right frontier of the fundamental sector.

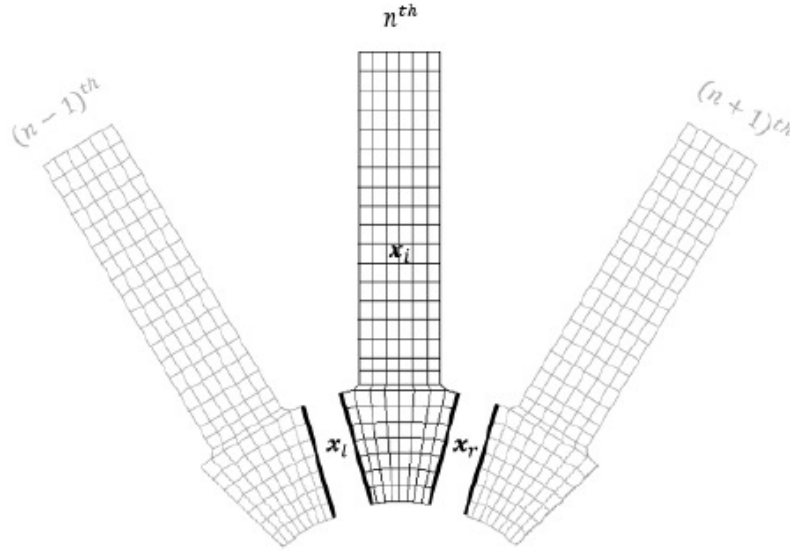


Figure 2.9: FEM sectors modelling [4].

Moreover, it is possible to state that the number of DOFs at the left and at the right frontier is the same and that the DOFs at the right frontier of one sector can be seen as the left ones of the following sector. Then, because of cyclic symmetry

$$\{x_r\} = \{x_l\}e^{i\varphi_n} \quad (2.28)$$

and the nodal vector can be written as:

$$\{x_s\} = \begin{Bmatrix} x_l \\ x_i \\ x_r \end{Bmatrix} = \begin{bmatrix} I & 0 \\ 0 & I \\ Ie^{i\varphi_n} & 0 \end{bmatrix} \begin{Bmatrix} x_l \\ x_i \end{Bmatrix} ; \quad \{x_s^n\} = [T^n] \begin{Bmatrix} x_l^n \\ x_i^n \end{Bmatrix} \quad (2.29)$$

where $[T^n]$ is the Mead's transformation matrix and $\{z_i^n\} = \{\{x_l^n\}^T \quad \{x_i^n\}^T\}^T$ is the vector of reduced nodals DOFs of the single vector. In an analog way, the force vector can be written as:

$$\{f_s\} = \begin{Bmatrix} f_l \\ f_i \\ f_r \end{Bmatrix}. \quad (2.30)$$

Thus, because of equilibrium:

$$\{f_r\}_n = -\{f_l\}_{n+1} \quad (2.31)$$

and for cyclic symmetry:

$$\{f_r\} = -\{f_l\}e^{i\varphi_n}. \quad (2.32)$$

Therefore, Mead's approach start from the model of an isolated sector consisting of $n_l + n_i + nr$ DOFs and leads to a reduced model with $n_l + n_i$ DOFs. In other words, by varying the value of φ_n it is possible to evaluate the dynamic behavior of the whole structure starting from the matrices of isolated sectors, thus making the whole modal analysis more simple and less time-consuming.

Modal families and FreND diagram

The dynamics of a bladed disk can be synthesized by mean of the *FreND diagram*, which represents the plot of the natural frequencies versus the number of nodal diameters characterizing the associated mode shapes. This diagram can be obtained performing several modal analysis varying the IBPA, and so the nodal diameter. Note that the number of natural frequencies of a discretized system is equal to its DOFs, while for a continuous system is infinite, this means that, in cyclic symmetry structures, for a given nodal diameter, the higher is the number of sector nodes, the higher is the number of natural frequencies that can be found. The most important blade modes can be seen in Figure 2.10 in which:

- **EW**: the blade tip moves axially;
- **FW**: the blade tip moves tangentially;
- **F**: the blade mid-span shows the maximum displacement;
- **T**: torsion around radial axis.

Thus, for a given cyclic symmetry structure, it is possible to plot the FreND diagram (Figure 2.11). As image shows, each modal family is represented by a line connecting

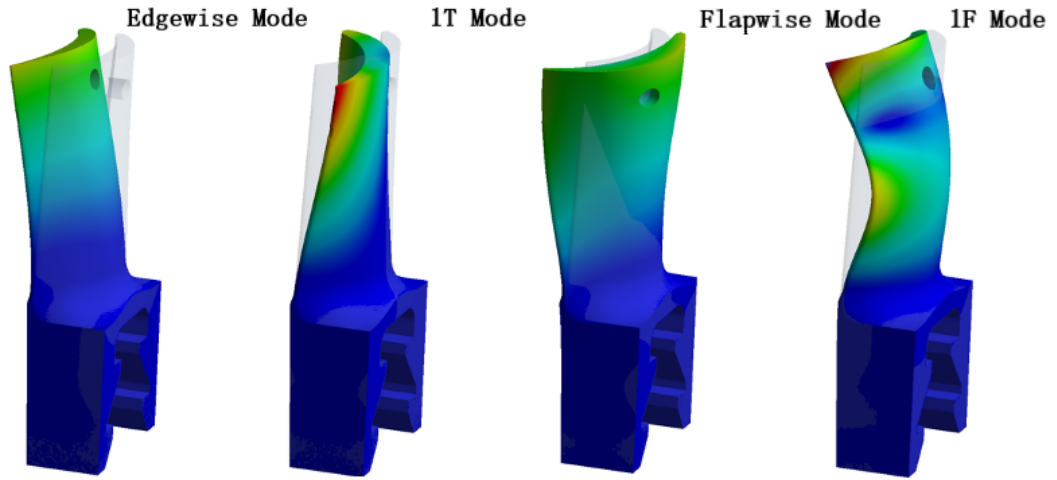


Figure 2.10: Blade mode shapes.

modes from $h = 0$ to \tilde{h} and modes having the same sector deformed shape (i.e. 1F-2F, 1T-2T,...) are grouped into distinct *families*.

Concerning the blade mode shapes, the number before the mode letter highlights the

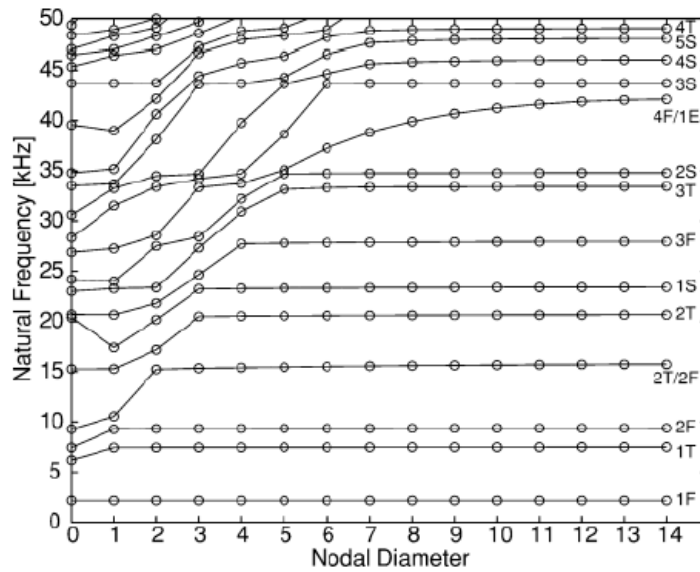


Figure 2.11: Example of FreND diagram.

number of semi-waves while the second one the number of mode for that semi-wave. Moreover, the higher is the number of nodal diameter, the lower is the natural frequency variation between that and the previous one. In fact, for low values of h , the blades are

dragged by the discs during vibration. As the number of nodal diameters increases, the disc becomes stiffer and the natural frequencies increases until the curves for each modal family asymptotically approach one natural frequency, which corresponds to that of the clamped, blade-alone configuration. Therefore, this portion of the diagram where quasi-horizontal curves are present is related with blade-dominated vibration modes, where the disk can be considered nearly motionless and the blades are weakly coupled among themselves.

In conclusion, it is possible that, for a given nodal diameter, 2 different modes have similar natural frequencies. This is called *veering* (Figure 2.12).

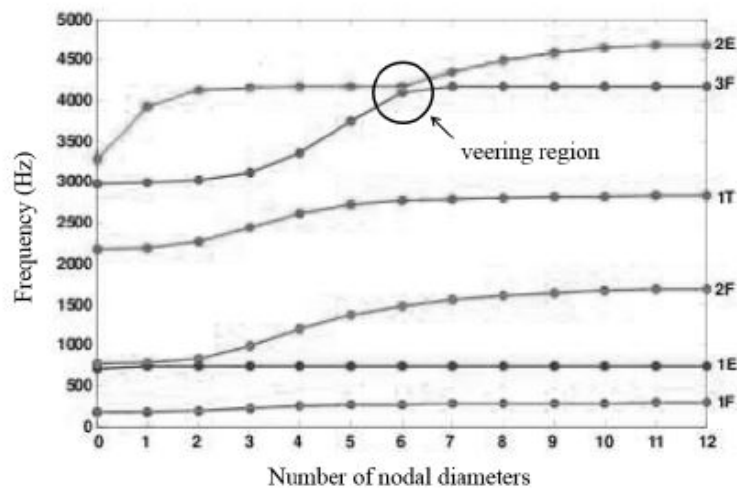


Figure 2.12: Veering region example [8].

2.3 Reduction techniques

The system described by the equation (2.1) is not easily resolvable. First, it is necessary to discretize a continuous system with infinite DOFs to a system with finite ones. This can be reached by FEM analysis that leads to the definition of a finite number nodes and elements and their relative formulations in order to get a system described by the equation (2.1). So, the problem moves towards the computational cost of inverting a matrix of dimension $n \times n$ where n is the number of DOFs of this system. In this perspective, several techniques are proposed to manage smartly this computation like LU decomposition and Cholesky factorization [15],[9], as well as the reduction techniques [10][2][3] in which a system of complexity n is reduced to another one of complexity m where $m < n$. In the latter technique, the DOFs vector is divided into *master* and *slave* coordinates and the relative mass and stiffness matrices are rearranged as well.

2.3.1 Modal reduction

Before introducing this reduction technique, *modal transformation matrix* will be defined for a given system of n DOFs as follows:

$$[\Psi] = [\{\psi_1\} \cdots \{\psi_n\}] \quad (2.33)$$

where $\{\psi_i\}$ is the i -th eigenvector. Defining $\{\eta\}$ as the *modal DOFs* of the system, it can be defined the relation:

$$\{x\} = [\Psi]\{\eta\} \quad (2.34)$$

So, the modal system becomes:

$$[M_{mod}]\{\ddot{\eta}\} + [K_{mod}]\{\eta\} = [\Psi]^T\{F\} \quad (2.35)$$

where $[M_{mod}]$, $[K_{mod}]$ are diagonal matrices composed respectively by modal mass and stiffness.

It can be assert that the modal system is uncoupled and so each equation can be studied as a system of one degree of freedom. Thanks to *superposition principle*, results from each equation can be combined.

Referring to the modal reduction, the system defined above can be reduced basing on the assumption that, for a specific condition (i.e. the operating one), only a limited subset of modes participate significantly to the motion and so it is possible to neglect the others. This means that, given a system of n DOFs and neglecting $n - m$ modes (where $m < n$),

the modal transformation matrix becomes:

$$[\Psi'] = [\{\psi_1\} \cdots \{\psi_m\}] \quad (2.36)$$

And so:

$$\{x\} = [\Psi]\{\eta\} \rightarrow \{x\} \simeq [\Psi']\{\eta\} \quad (2.37)$$

Thus the modal system becomes:

$$[M_{red}]\{\ddot{\eta}\} + [K_{red}]\{\eta\} = [\Psi']^T\{F\} \quad (2.38)$$

where $[M_{red}]$, $[K_{red}]$ are diagonal matrices composed respectively by modal mass and stiffness, in fact, neglecting modes doesn't change diagonability because of $[\Psi]$ transformation. This simplified approach leads to two main sources of errors:

- error due to neglected $n - m$ modes;
- not consider the modal coupling due to damping in fact under the hypothesis of non proportional damping, the quantity $[\Psi']^T[C][\Psi']$ is not diagonal.

Chapter 3

Aeromechanical instabilities

When considering a turbine rotor, aeromechanical instabilities must be taken into account. One of the most important among these is *flutter* that occurs when, following an initial structure displacement, the fluid enhances the vibration. The consequential increment in amplitude may lead to structure rupture long before than the classical fatigue analysis prediction. The discipline that studies the interaction between the modal behavior of a structure and the fluid flow is called *Aeroelasticity* and it can be described as the interaction between 3 different fields according to the *Collar triangle* [13].

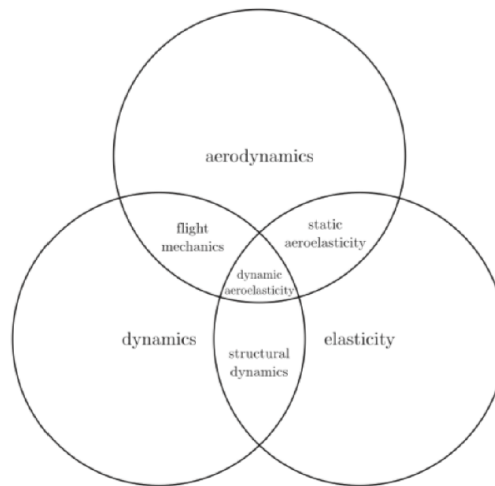


Figure 3.1: Collar's triangle.

As shown (Figure 3.1), the also known *Collar Diagram* is composed by several areas:

- Structure dynamics: discipline where inertial and elastic forces are considered (Vibration mechanic);
- Flight Mechanic: with inertial and aerodynamic forces (Aerodynamic stability);

- Static aeroelasticity: when elastic and aerodynamic forces are present (Divergence);
- Dynamic aeroelasticity: all fields are included, elastic inertial and aerodynamic forces (Forced response and flutter).

In general, the aerodynamic field represents the excitation source while elastic and inertial fields represents the system response. The flutter phenomenon falls in the subcategory of dynamic aeroelastic stability problem. Its origin may be related to the detachment of the fluid flow from the airfoil (case of *Stall Flutter*), or to the detachment of the wake vortex from the LE (*Transonic buffeting*) which both cause auto-excited vibrations. In turbine rotors usually only Stall Flutter is analyzed since the other types of flutter are not considered to be dangerous from a structural point of view.

3.1 Aerodynamic of turbines

A better comprehension of matters related with aeromechanical instabilities requires the knowledge of Aerodynamic of turbines that, despite the more traditional 1D formulation of an airfoil hit by air, cannot be described without neglecting multi-dimensional aspects [6] since the motion field is affected by interactions between rotating and non rotating parts (stator and rotor), centrifugal forces as well as wall effects.

Whenever high pressure gradient occurs between upstream and downstream of an airfoil, vortexes can be generated leading to one of the most important phenomenon that affects turbine's aerodynamic: the "stall condition" in which the main flow is *stalled* forcing the fluid flowing in the near regions to accelerate and so increasing the crossing speed at the midspan.

Other cases in which vortexes are generated are the ones that occur when the wall flow encounter the fluid at the stagnation condition. In this case it can be observed a couple of vortexes that shows a different behavior depending if those are in the suction side (vortexes remain attached to the airfoil due to blade motion) or in the pressure side (those continue to proceed axially but moving towards the adjacent blade interacting also with the main fluid stream).

In addition, the high gradient of the pressure field creates secondary flows between stator and rotor blades that cross the entire stages until the downstream region. Those secondary flows interact with high and low pressure regions creating vortexes.

The above-mentioned phenomena, which are source of the aerodynamic losses with an high impact to the turbine efficiency, may lead to unsteady condition.

Potential disturbs

Under the hypothesis of *irrotational motion field*, i.e. $\nabla \times \bar{u} = 0$, the velocity field flowing around an airfoil profile can be described by the gradient of a potential function. Moreover, according to the Kutta-Joukowski theorem, if the circulation around an airfoil profile, defined by the equation (3.1), is different from 0, then there will be a change of the velocity field also at the upstream and downstream. As a consequence, unsteady pressure generates disturbs in terms on pressure waves which propagates at the upstream and downstream. These are characterized by an exponential decay governed by the Mach number, the pitch and axial distance.

$$\Gamma = \oint_{air\ foil} \bar{u} \cdot \hat{n} dl \quad (3.1)$$

Shock waves

Shock waves are a type of propagating disturbance faster than the local medium speed of sound that occurs when there is a stream discontinuity between sub-sonic and super-sonic velocity. In these conditions the thermodynamic properties (pressure, temperature, density) change drastically generating shock waves which can propagate horizontally or obliquely. The main source for the former are generally choking conditions (a situation in which the critical pressure is reached and the fluid flow results *choked*); oblique shock waves depend, instead, by the flow deflection and by the Mach number. Whenever downstream condition changes the flow characteristic curve changes too, generating a sort of pressure jump (discontinuity) in a local region. This phenomenon creates a pressure horizontal wave that preserve flow energy but increase entropy.

Wakes

Wake can be defined as the region of disturbed flow (often turbulent) downstream of a solid body moving through a fluid, caused by the flow of the fluid around the body (Figure 3.2). It occurs due to the not negligible pressure gradient related to fluid viscosity. The wake area affects the surrounding flow field, modifying its velocity components and so aerodynamic efficiencies. Moreover, during the fluid motion, the wakes are modified by the pressure fields characterizing a circumferential a-periodicity when the fluid returns to the original reference system.

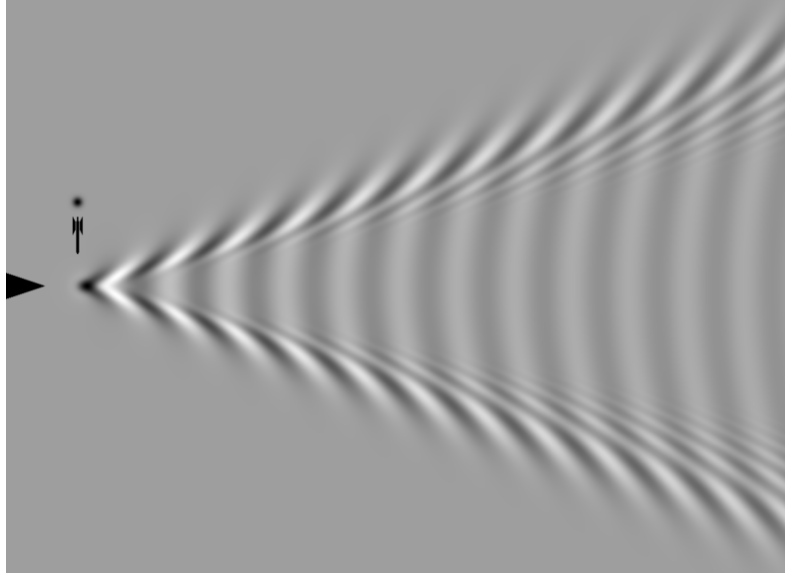


Figure 3.2: Example of wake [29].

3.2 Aeroelasticity in turbomachines

Aeroelasticity is the branch of engineering that studies the mutual interaction between aerodynamic forces, structural dynamics and elasticity leading to a change of stability condition of an aeromechanical system. Referring to steady condition (static aeroelasticity), stability is achieved when there is equilibrium between elastic forces and aerodynamic ones. If it does not happen, *divergence* (which can be seen like Euler instability [11]) occurs, causing amplified strain of structure which can bring to its damage.

3.2.1 Flutter

Flutter is the most important phenomena linked with dynamic aeroelasticity. It is caused by asynchronous vibrations (see next chapter) and, when it occurs, aerodynamic forces produce an excitation to the system which self excite the structure. Under an energetic point of view it is possible to define the work per cycle of an exciting force as:

$$W_{cycle} = \int_t^{t+T} \int_S -p\hat{n} \cdot \vec{v} dS dt \quad (3.2)$$

If $W_{cycle} > 0$ the system is stable, if $W_{cycle} < 0$ the system is unstable. The former case occurs when force obstructs motion and vice versa: damping turns up.

Classic flutter

The above-mentioned *Stall Flutter* is a complex phenomenon and it can be described in according to various physical models. However, in the current thesis, only the *Classic Flutter semi-stationary model* will be considered. This is based on the idea that, once the airfoil motion is known, it is possible to express the aerodynamic forces as functions of $h, \theta, I_h, I_\theta, m_h$ and m_θ . As flutter takes place when the real part of the system's eigenvalue becomes null, the blade's motion can be assumed purely harmonic. It is possible to express the vector of the aerodynamic forces as:

$$\{F_a(t)\} = M_a\{\ddot{x}\} + C_a\{\dot{x}\} + K_a\{x\}, \quad (3.3)$$

where the vector $\{x\}$ contains the coordinates h and θ (see Figure 3.3) and the matrices M_a , C_a and K_a represent, respectively, the aerodynamic inertia, damping and stiffness of the system. Considering a generic multiple DOF system like the one shown below, the governing equation can be written as:

$$M\{\ddot{x}\} + C\{\dot{x}\} + K\{x\} = \{F_m(t)\} + \{F_a(t)\}. \quad (3.4)$$

At this point, using the hypothesis that all the external loads that are not of aerodynamic nature can be neglected ($\{F_m(t)\}$) and replacing the second term of the right hand side with the expression in Equation (3.3), the following equation can be obtained:

$$(M - M_a)\{\ddot{x}\} + (C - C_a)\{\dot{x}\} + (K - K_a)\{x\} = 0. \quad (3.5)$$

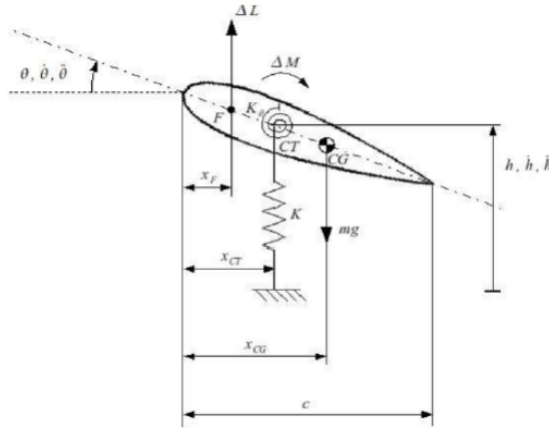


Figure 3.3: Example of a 2 DOF system.

General solution of the above equation (3.5) can be written as follows:

$$\{x(t)\} = \{\bar{x}_j\}e^{s_j t}, \quad (3.6)$$

where s represents the eigenvalue and it is a complex number:

$$s_j = \zeta_j + i\omega_j. \quad (3.7)$$

The term ω_j governs the frequency of the system ($e^{st} = e^{\zeta + i\omega} = e^{\zeta t} \cdot e^{i\omega t}$ and $e^{i\omega t} = \cos(\omega t) + i \sin(\omega t)$), while ζ_j expresses the stability of the system:

- if $Re(s) > 0$ the system is unstable (Figure 3.4);
- if $Re(s) = 0$ the system is oscillatory (Figure 3.5);
- if $Re(s) < 0$ the system is asymptotically stable and shows an exponential decay (Figure 3.6).

Since $\zeta = f(velocity)$ and flutter occurs when $\zeta > 0$, there will be a $v_{critical}$ that defines the dividing line between stable and unstable region.

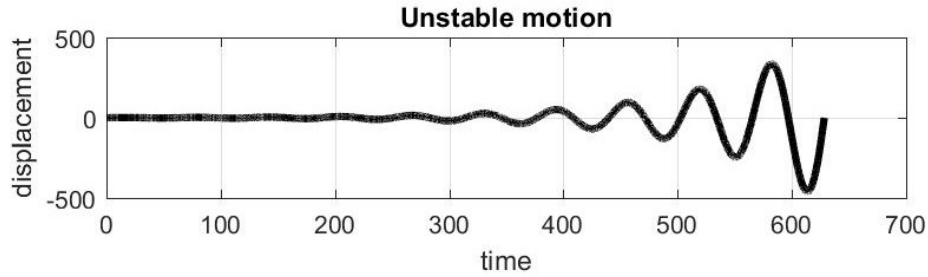


Figure 3.4: Unstable system response.

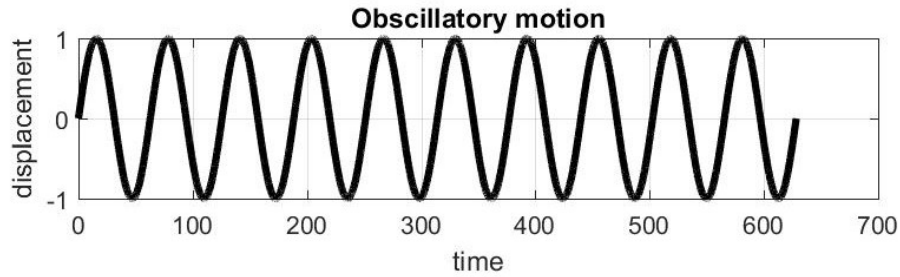


Figure 3.5: Oscillatory system response.

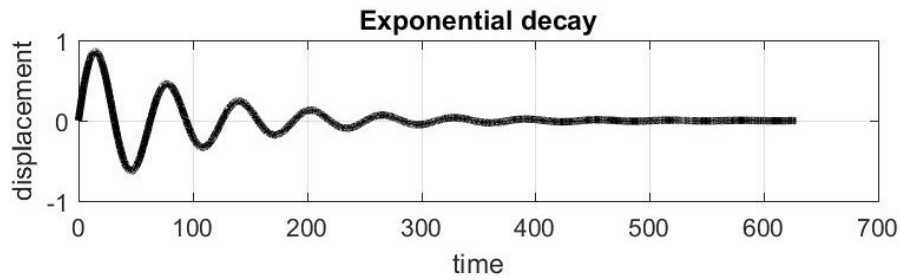


Figure 3.6: Stable system response.

Flutter in turbomachines

Considerations applied for the single airfoil profile in the previous section, can be extended to the whole rotor flow taking into account the coupling of disturbances between blades. The so-known *aerodynamic coupling* [20] causes that a disturbance on one blade will not only change the conditions of the flow that surrounds it but it will move around the rotor and affect the neighboring blades (Figure 3.7). A further interaction takes place between

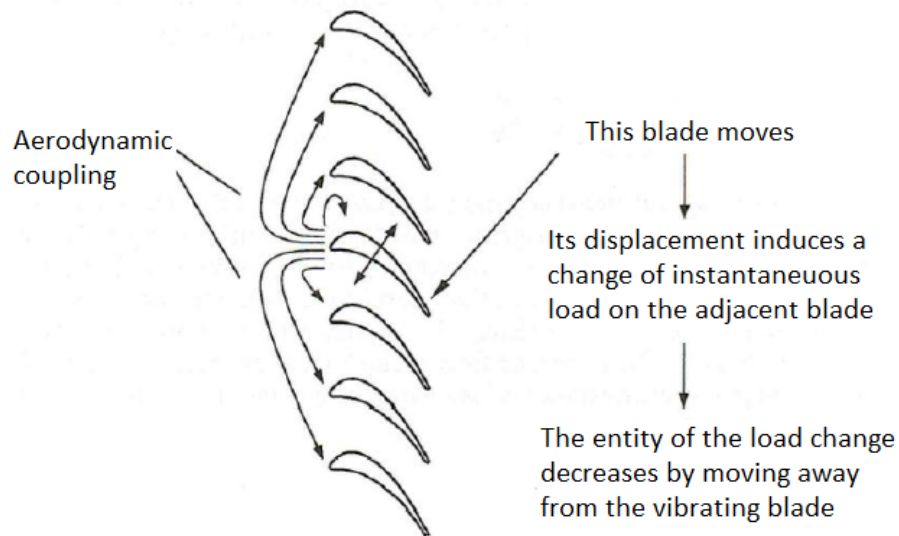


Figure 3.7: Aerodynamic coupling on a blade row.

rotor and stator where angle of incidence, together with flow's velocity and blade's mode shapes, will play a crucial role in the possible occurrence of flutter.

According to A.V. Srinivasan [23], the most important parameters affecting flutter are:

- IBPA: is the angle representing the phase shift between adjacent blades during their

vibration motion. It defines the characteristics of the coupling among the blades.

- Shroud: contact between adjacent blades shrouds introduces a certain damping due to friction forces that modifies the modal shapes and loads at the interface.
- Shock waves: strongly influence the pressure load at leading edge.
- Inlet and outlet conditions: pressure and temperature affects the aerodynamic damping.
- Reduced frequency: defined as the ratio between the axial semi-chord and the time needed for the aerodynamic profile to complete a full vibration cycle:

$$k = \frac{c\omega}{2V}. \quad (3.8)$$

When this parameter is low, the flow can be considered quasi-static, otherwise it is unsteady.

- Mistuning: it is based to non-homogeneity between blades which modifies mass and stiffness of blades in order to modify the aerodynamic coupling reaching flutter stability.

In order to analyze the flutter stability it is necessary to understand how blades interact from both an aerodynamic and a structural point of view. Even though in this thesis the detailed process will be not explained, the approach requires the knowledge of blades' displacements. Thus, a previous modal analysis is needed basing on the hypothesis that the influence of gas flow on natural frequencies and mode-shapes can be neglected.

As written above, flutter instability can be identified thanks to aerodynamic damping coefficient ζ . If this parameter has a negative value, the structure is not able to dissipate energy: unstable aeroelastic condition. *Aerodynamic coupling* represents the influence of near vibrating blades as written in the lines above. ζ , as a function of the IBPA, can be a valid parameter to understand of how blades influence each other vibration (Figure 3.8). It is possible to observe that if a single oscillating blade is considered (blade 0), the aerodynamic damping is obviously constant with respect to the IBPA. Instead, considering more blades, flutter instability is influenced by the value of the IBPA and shows a sinusoidal trend. Moreover, the farther is the blades (example of blades with indices ± 2) respect to the reference one, the lower is the influence.

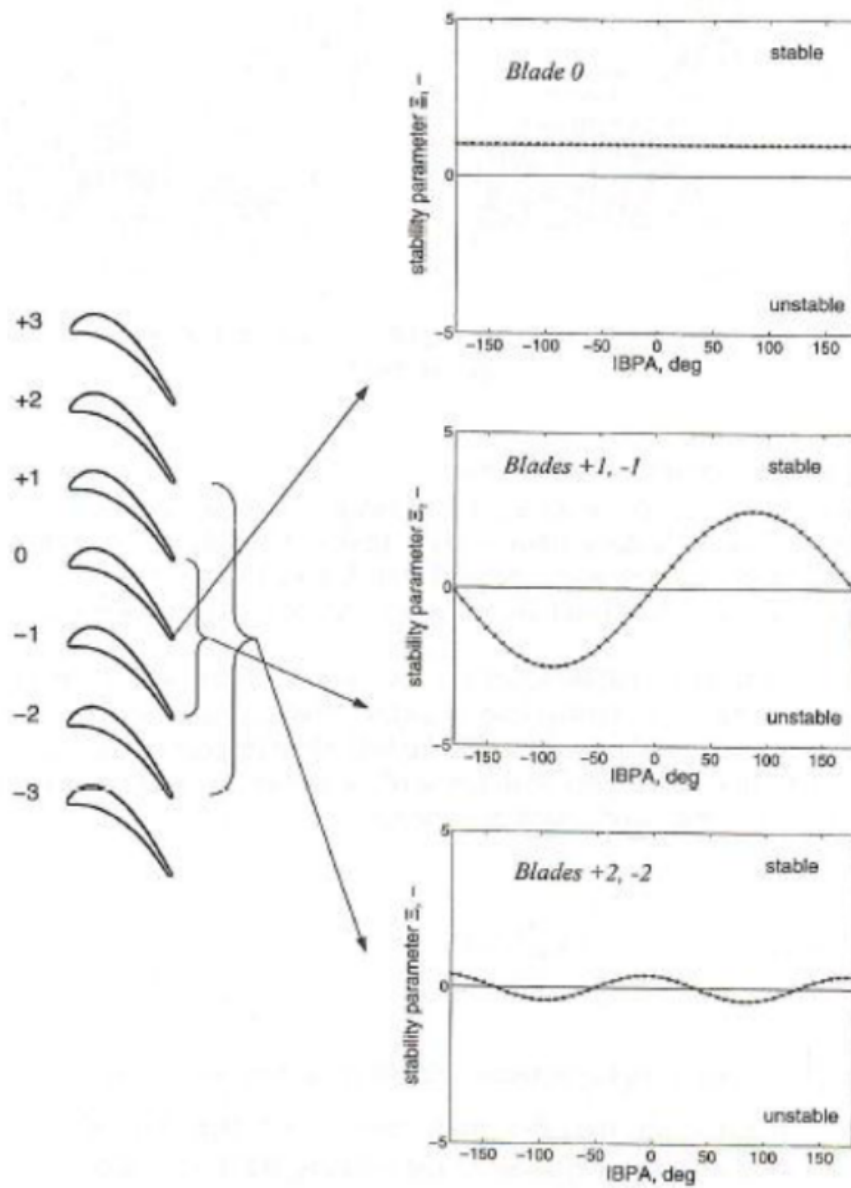


Figure 3.8: Aerodynamic coupling as function of IBPA.

Furthermore, assuming, in a row in which all blades are vibrating, small displacements and thus that the system is linear, it is possible to apply the superposition principle. Thanks to this assumption, damping coefficient variation versus the IBPA is commonly represented by the *aeroplots* showed in Figure 3.9.

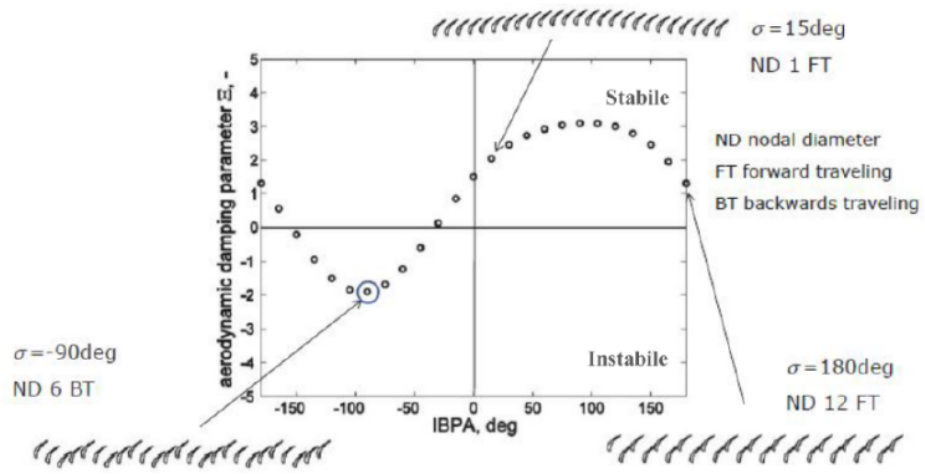


Figure 3.9: Example of aeroplots.

Chapter 4

Forced Response

4.1 Static and Dynamics loads

According to Maggiore, Moletta et al. [17], the main excitation sources affecting a Low Pressure Turbine can be classified in: *static loads* made by constant or limited time variation forces; *quasi-static loads*: forces with constant temporal characteristics but related with dynamic phenomena; *dynamic loads*: time-depending forces. Note that the lasts can be considered static if compared with a much higher natural frequency, otherwise loads can be considered dynamic. Thus, what really matters is the natural frequency of the system compared to the frequency of excitation source.

The main static loads of LPT are four:

- Steady pressure field: linked with a different pressure field between suction side and pressure side due to the gas-flow passing along blades. Defining with p the pressure field and with S the blade surface, the resultant force can be computed as:

$$F_p = \int_S p \hat{n} dS. \quad (4.1)$$

- Inertial load: rotating parts are subjected to centrifugal force expressed by the following equation:

$$F_c = \int_m dF_c = \int_V \rho \omega^2 r \hat{\mu}_r dV. \quad (4.2)$$

- Temperature load: deriving from the hot gases that not only transfer energy to blades under the form of mechanical work, but also warm them creating a high thermal gradient which leads to creep phenomena.
- Pre-Twist load: a kind of pre-loading of blades due to achieve the right position of the airfoil respect the gas flux.

Time-depending forces in a LPT may have many sources. Generally they origin from unsteady pressure field and the harmonic terms are function of blades' number and angular velocity. In this case, dynamic excitations induce *synchronous vibrations*. Differently other dynamic loads' sources are linked with flux instability as separations, vortex shedding or rotor stall. Excitations originated by these cases do not show frequencies that are multiplies of rotational speed of the system: *a-synchronous vibrations*.

Talking about the former, those harmonic forces are identified by a parameter called *Engine Order* defined as:

$$EO = \frac{\omega}{\Omega}. \quad (4.3)$$

Generally, forced response can be associated to high EOs or low EOs. First case is caused by the interaction between rotor and stator row; second one concerns to high nodal diameter discontinuities like unbalanced rotating masses, asymmetry in tree's supports, interaction with distorted flow arriving from combustor.

Returning to the generic excitation with synchronous vibrations, thanks to periodicity, it is possible to apply the Fourier series in order to represent it:

$$F(\alpha) = F_0 + \sum_{eo} F_c^{(eo)} \cos(eo \cdot \alpha) + F_s^{(eo)} \sin(eo \cdot \alpha), \quad (4.4)$$

where $\alpha = \omega t$ and eo is the engine order.

So that, most of the dynamic loads (with the exception of mechanical impacts and self-excited phenomena) induce synchronous vibrations since that excitation frequency depends on the rotational speed. Moreover, natural frequencies of a rotor-dynamical system depend on the rotational speed, especially due to stiffening induced by large centrifugal forces.

In this overview, Wilfred Campbell provided an important contribute. In fact, in order to study the forced response of a bladed disk, *Campbell's Diagram* is commonly used (Figure 4.1). In the diagram, with rotation speed on horizontal axis and frequency on the vertical one, the natural frequencies are represented as a set of lines which trend depends on the rotation speed, while the EO excitation frequencies are represented by straight lines starting from axis origin. Potential resonance situations occur when excitants' curves cross the ones of natural frequencies. However crossing is a necessary but not sufficient condition to resonance.

In particular, the critical intersections are those for which the following relations holds:

$$EO = m \cdot N \pm ND \quad (4.5)$$

which can be graphically represented by the zig-zag diagram 4.2.

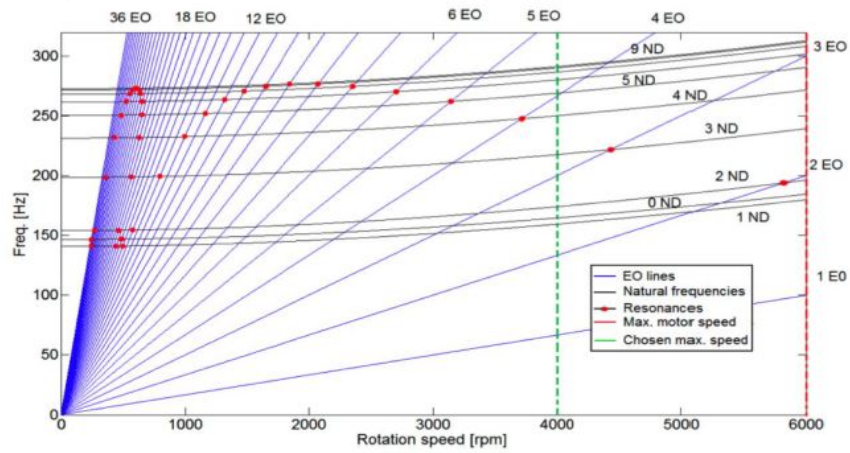


Figure 4.1: Example of a Campbell diagram [16].

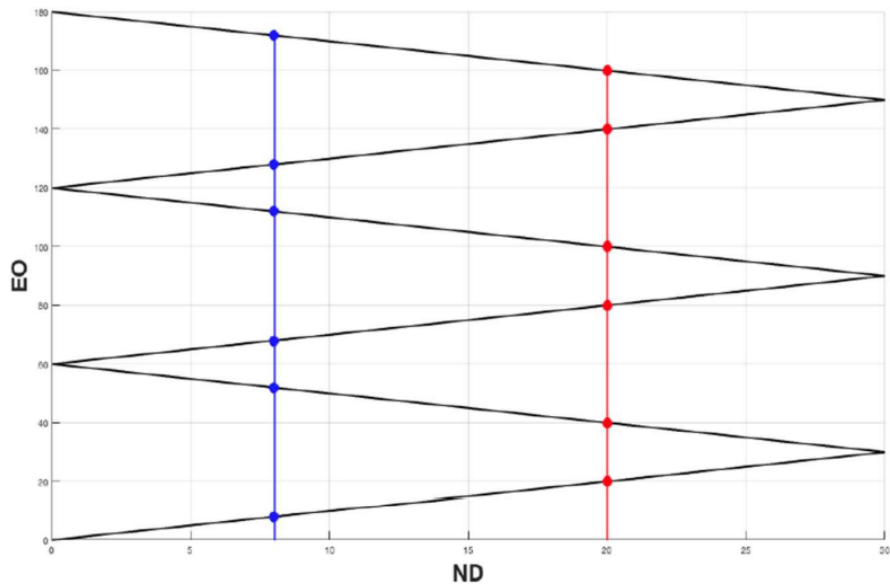


Figure 4.2: Zig-zag diagram.

Equation 4.5 demonstrates that resonance response can occur also when $m \neq 0$ due to *aliasing phenomenon*: since the rotor blades represent a discrete system they can be forced in a finite number of points; higher value EOs are detected by the system with reduce frequencies. These shifts depend on the number of discretized sectors. Thus, the

resonance condition can be expressed as follows:

$$EO' = EO - m \cdot N = ND \quad (4.6)$$

To a better understanding of this phenomenon, refer to the Figure 4.3 in which two different periodic functions ($EO = 4$ and $EO = 17$) show same values (red dots) and so effects. As *zig-zag diagram* shows, different EOs put in resonance the same nodal diameter. In this example, if an excitation with $EO = 4$ represents a resonance condition, the same occurs with the one of $EO = 17$, since this force is seen by the row of blades as a wave characterized by $EO = 4$ (obviously this EO is able to excite in resonance condition a mode shape with $ND = 8$).

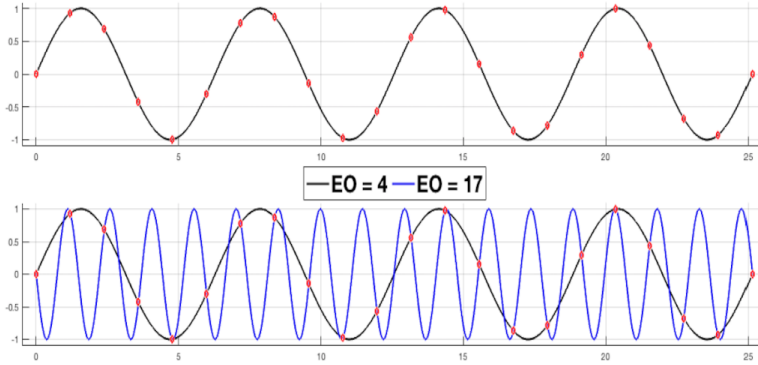


Figure 4.3: Aliasing.

The Campbell diagram is useful during the design phase in order to highlight different resonant conditions which have to be matched with the operating condition of the Low Pressure Turbine. Whenever possible resonances may occur, the rotational speed or the natural frequencies will be modified in order to manage this problem.

Chapter 5

Dynamical Analysis of Multistage Cyclic Structures

Aircraft engines are made up of different rotational periodic structures such as turbine bladed disks or gear wheels (Figure 5.1; Figure 5.2). It is well known that the dynamics of such structures can be studied using the cyclic symmetry reduction. Using this method (explained in the Section 2.1), a complete cyclic structure can be analyzed considering a single elementary sector. Starting from the early developments of cyclic symmetry structure [24], there are numerous examples in the literature on this subject. Nevertheless, although some applications involve assemblies made up of cyclic structures leading to a multistage pattern (i.e. compressors or turbines), most existing studies focus on single stage analysis neglecting the influence of the interstage. One of the consequences of this carelessness can be the underestimation of vibratory levels.

Despite this problem, the cyclic symmetry reduction cannot be applied directly to the multistage assembly; so that, full 360 models are required to study the dynamics of multistage systems often leading to prohibitive computation costs.

In the present thesis work, we focus on a new strategy to study the dynamics of multistage assemblies using a cyclic symmetry reduction. The method presented in the next section, handles the sector finite element cyclic modeling of each stage and involves a realistic interstage coupling.

5.1 Multistage Cyclic Symmetry method

Referring to the above-mentioned problems, in this section a strategy to analyze the dynamics of multistage cyclic structures is presented. The interstage coupling is ensured through a cyclic expansion of the interface DOFs of each stage. Methodology will be

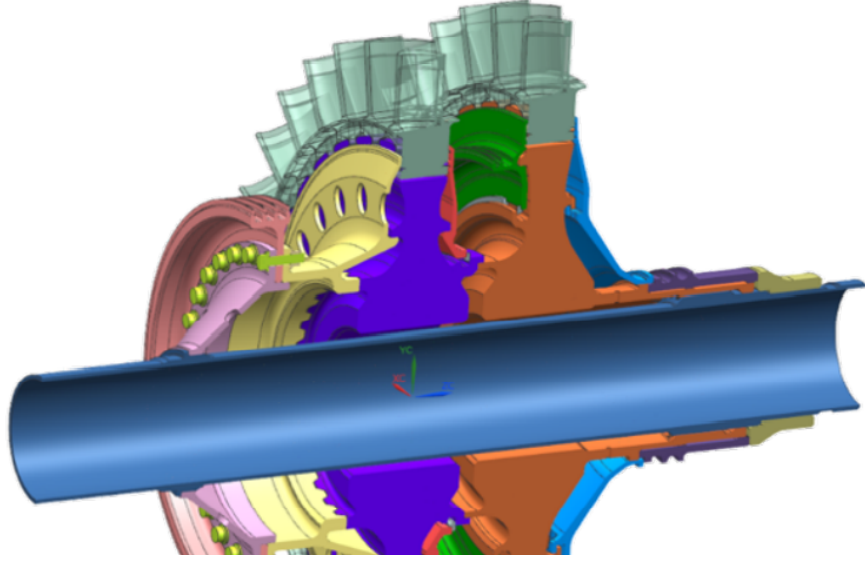


Figure 5.1: Turbomachinery Multistage Cyclic Structure [18].

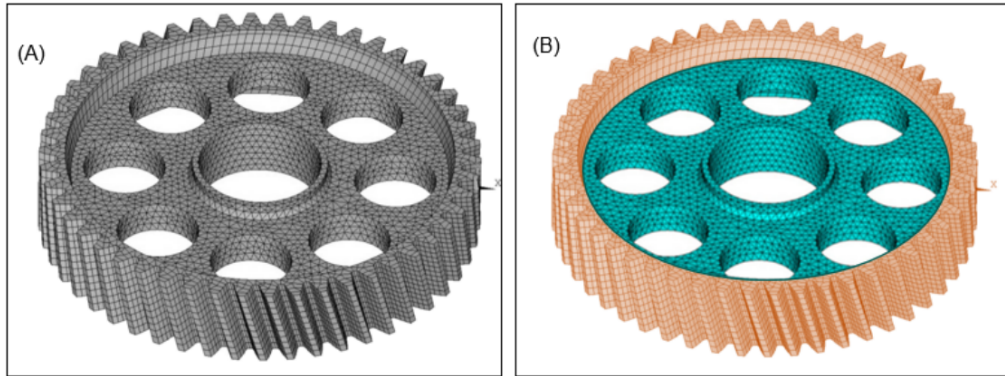


Figure 5.2: Gear (A) modeled as a Multistage Cyclic Structure with two stages (B) [18].

detailed based on two stages composed of N_1 and N_2 sectors ($N_1 \neq N_2$), but can be easily extended to more stages. Furthermore, mesh compatibility is assumed for the interstage coupling, but, it is important underline that, in case where interfaces would not match, a solution can be the use of multi-point constraints.

First, we will define for both stages the vector containing the degrees of freedom of the reference sector in physical ($\mathbf{u}_n^{(i)}; i = 1,2$) and cyclic bases ($\tilde{\mathbf{u}}_n^{(i)}; i = 1,2$). The latter coordinates are used in each reduced problem and the transformation in physical coordinates is given by:

$$\mathbf{u} = \mathbf{e}_n \otimes \tilde{\mathbf{u}} \quad ; \quad \mathbf{e}_n = \left[1 \quad e^{\frac{2i\pi n}{N}} \quad e^{\frac{4i\pi n}{N}} \quad \dots \quad e^{\frac{2(N-1)i\pi n}{N}} \right]^T \quad (5.1)$$

where \otimes is the Kronecker product (or matrix direct product). Then, we will indicate, in physical and cyclic bases, ${}^b\mathbf{u}_n^{(i)}$ and ${}^b\tilde{\mathbf{u}}_n^{(i)}$ DOFs referring to the interstage of each stage. All DOFs different from these will be designated as ${}^o\mathbf{u}_n^{(i)}$ and ${}^o\tilde{\mathbf{u}}_n^{(i)}$. Additionally, the following identity matrices are necessary: I_{b_i} and I_{o_i} which size correspond to the number of boundary and internal DOFs of i -th stage.

Referring to the physical base, to ensure compatibility, the boundary degrees of freedom between stages are enforced to be equal. So that:

$${}^b\mathbf{u}^{(1)} = {}^b\mathbf{u}^{(2)} \quad (5.2)$$

Then, according to (5.1), we have:

$${}^b\mathbf{u}^{(1)} = (\mathbf{e}_{N_1,n} \otimes I_{b_1}) {}^b\tilde{\mathbf{u}}_n^{(1)} \quad \text{and} \quad {}^b\mathbf{u}^{(2)} = (\mathbf{e}_{N_2,n} \otimes I_{b_2}) {}^b\tilde{\mathbf{u}}_n^{(2)}$$

Using cyclic coordinates, (5.2) can be rewritten as:

$${}^b\tilde{\mathbf{u}}_n^{(2)} = B_n {}^b\tilde{\mathbf{u}}_n^{(1)} \quad \text{with} \quad B_n = (\mathbf{e}_{N_2,n}^* \otimes I_{b_2})(\mathbf{e}_{N_1,n} \otimes I_{b_1})$$

The matrix B_n is the projection matrix of the n -th cyclic vector of stage 1 on the n -th cyclic vector of stage 2. At this point, assembling the two stages degrees of freedom vector, the eigenvalue problem can defined (5.3):

$$\begin{bmatrix} \tilde{\mathbf{u}}_n^{(1)} \\ \tilde{\mathbf{u}}_n^{(2)} \end{bmatrix} = T_n \tilde{\mathbf{u}}_n^{(1\cup 2)} \quad \text{with} \quad T_n = \begin{pmatrix} I_{b_1} & 0 & 0 \\ 0 & I_{o_1} & 0 \\ B_n & 0 & 0 \\ 0 & 0 & I_{o_2} \end{pmatrix} \quad \text{and} \quad \tilde{\mathbf{u}}_n^{(1\cup 2)} = \begin{bmatrix} {}^b\tilde{\mathbf{u}}_n^{(1)} \\ {}^o\tilde{\mathbf{u}}_n^{(1)} \\ {}^o\tilde{\mathbf{u}}_n^{(2)} \end{bmatrix} ;$$

$$K_n^{(1\cup 2)} \tilde{\mathbf{u}}_n^{(1\cup 2)} = M_n^{(1\cup 2)} \tilde{\mathbf{u}}_n^{(1\cup 2)} \lambda \quad (5.3)$$

with

$$K_n^{(1\cup 2)} = T_n^T \begin{pmatrix} K_n^{(1)} & 0 \\ 0 & K_n^{(2)} \end{pmatrix} T_n \quad \text{and} \quad M_n^{(1\cup 2)} = T_n^T \begin{pmatrix} M_n^{(1)} & 0 \\ 0 & M_n^{(2)} \end{pmatrix} T_n$$

Using this method, the size of problem is close to the sum of the two individual stages problem sizes. If the interstage boundary DOFs are not aligned, a mapping matrix is applied to relate interstage boundary DOFs.

5.2 Multistage Cyclic Symmetry application

In order to perform the above-described method, a *commercial fem tool*, capable to provide a way to combine two or more independent cyclically symmetric systems with different sector counts, will be used.

The functionality of the Multistage Cyclic Symmetry application can be summarized in the following example:

- Modeling of different stages with different sectors counts (Figure 5.3) without the need of a 360 full model (lowering of computational costs).
- Figure 5.4 shows a possible rotating stage attached to the driving axle of an aircraft engine. This stage is made up of 43 sectors. In order to modeling the connections with the rotating tree, we will refer to the drilled part shown in the Figure 5.5. Supposing that 18 screws are used to tie together stage and rotating tree, using Multistage Cyclic Symmetry is the best way to modeling this problem since stages can have different number of sectors. Further, as written above, if the interstage boundary DOFs are not aligned, a mapping matrix is applied to relate them and connect the two stages through their interface.

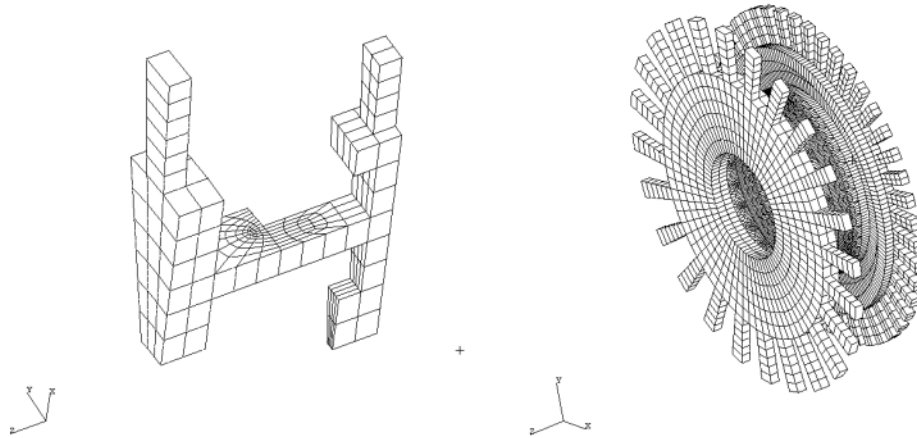


Figure 5.3: Finite element model of 2 cyclic structures with 24 and 45 sectors [14].



Figure 5.4: Example of a sector from a rotating stage.

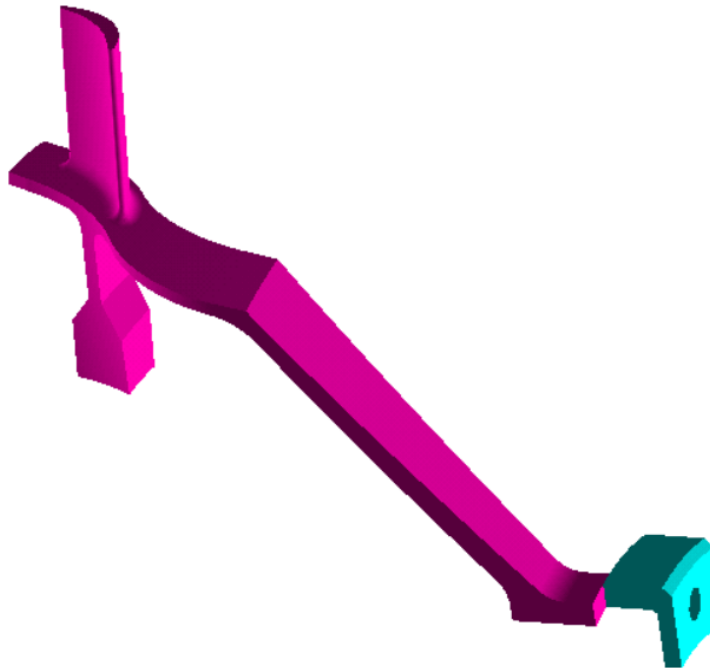


Figure 5.5: Example of a sector from a rotating stage with a drilled part.

Regarding the last example shown in the Figure 5.5, a *commercial fem tool* will be used here to run a modal analysis. Since we want to model a rotating stage attached to the driving axle, displacements along *z-axis* and *y-axis* (a *z-axis* cylindrical coordinate system is set - Figure 5.7) are not allowed for the nodes of the drilled part FEM model on the inner radius (minimum *y* coordinate) (Figure 5.6).

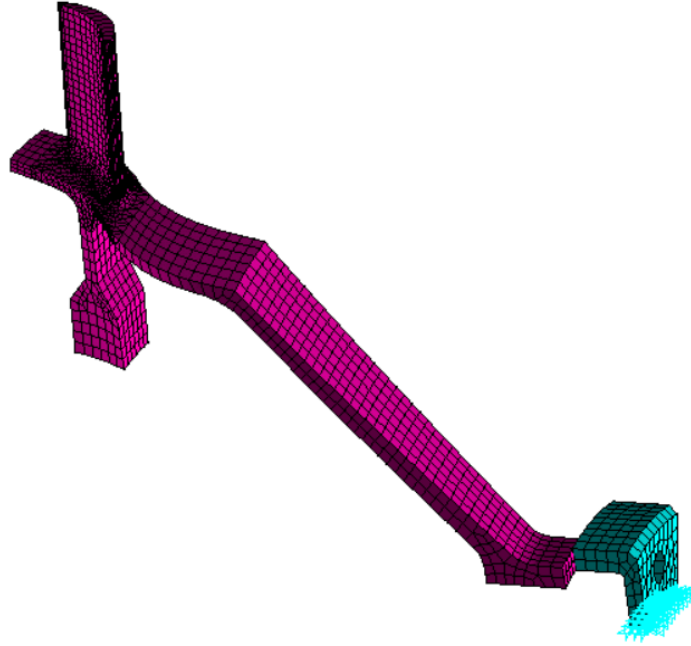


Figure 5.6: Nodes whose displacements along *z-axis* and *y-axis* are forbidden.

Running the modal analysis with a *harmonic index* equal to 0, we will obtain the results showed in the Figure 5.7. As we can see, $HI = 0$ is related with real modes where all the blades vibrate in phase (when HI has different values from 0 or $N/2$, with N equal to the number of sectors, it is related with complex modes). Additionally, results show how a 360 full model is not required since using the above-mentioned method we can obtain the modal shapes with a much lower impact on computational costs (in terms of execution time and memory used).

Other consideration are related with the unmatched nodes or elements at the interstage boundaries of adjacent stages (note that in Figure 5.6). The used *fem tool* assures the constraint equations (and so the continuity) between interstage nodes.

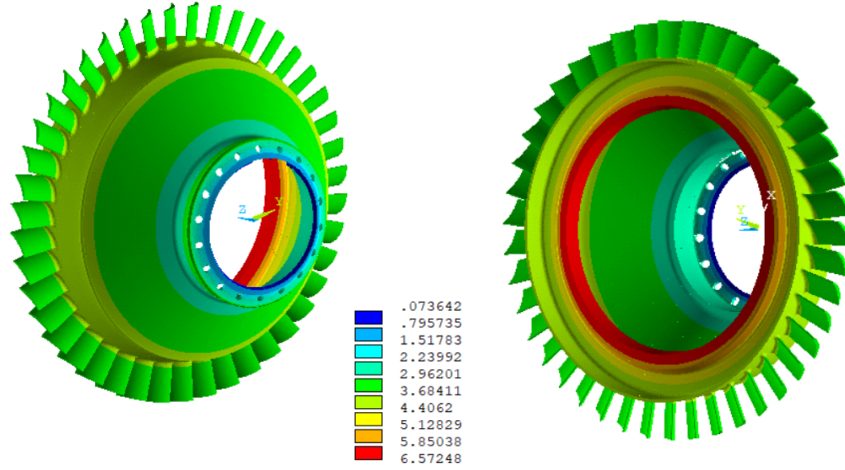


Figure 5.7: Modal shape, Harmonic Index equal to 0 , Frequency = 617.8 Hz , Displacements in [mm] - back and front view -.

5.3 Modal Assurance Criterion (MAC)

In order to check the goodness of results obtainable using the above-mentioned method, Modal Assurance Criterion (MAC) calculation is presented here. MAC is a statistical indicator that is most sensitive to large differences and relatively insensitive to the small ones in mode shapes. It is important to underline that MAC considers only modal shapes without referring to frequency comparison (usually used in conjunction with MAC). In this thesis, it will be used as a degree of consistency between mode shapes derived from a 360 full model with those obtained from Multistage Cyclic Symmetry application. MAC is bounded between 0 and 1, with 1 indicating fully consistent mode shapes while 0 not consistent ones.

Since mode matching is an important and essential step before undertaking any comparison, there are several modal properties that are related to it, including natural frequencies, real mode shape vectors, modal masses, modal kinetic and strain energies and, for complex modes, modal damping ratios and complex mode shapes. Between these, one of the most popular tools for the quantitative comparison of modal vectors is the above-mentioned Modal Assurance Criterion.

5.3.1 MAC calculation

The MAC is calculated as the normalized scalar product of the two sets of vectors $\{V_A\}$ and $\{V_B\}$. Scalar results are arranged in the *MAC matrix* [19]:

$$MAC(r, q) = \frac{|\{V_A\}_r^T \{V_B\}_q|^2}{(\{V_A\}_r^T \{V_A\}_r)(\{V_B\}_q^T \{V_B\}_q)} ; \quad (5.4)$$

the previous equation can be reformulated for complex modes of vibration as:

$$MAC(r, q) = \frac{|\{\Psi_A\}_r^T \{\Psi_B\}_q^*|^2}{(\{\Psi_A\}_r^T \{\Psi_A\}_r^*)(\{\Psi_B\}_q^T \{\Psi_B\}_q^*)} ; \quad (5.5)$$

and is clearly a real quantity, even though related to complex mode shapes.

As explained before, MAC takes value from 0 (in case of no consistent correspondence) to 1 (representing the case in which mode shape pairs exactly match). However, value larger than 0.9 can be related to the latter case, indicating great resemblance of the two shapes. Note that, MAC can take a value near unity even if the following reasons occur: number of response DOFs is insufficient to distinguish between independent mode shapes; mode shapes are a result of unmeasured forces to the system; mode shapes represent the same motion different only by a scalar. Thus, results of a modal assurance criterion calculation must be carefully interpreted, remembering that MAC can only indicate consistency and not validity. As a consequence, it is mainly used in pre-test mode pairing.

Magnitude data from MAC analysis are often represented through 2D or 3D plot (Figure 5.8). Considering that MAC is a discrete calculation, what is highlighted with a color contour plot only represents the discrete mode to mode comparison.

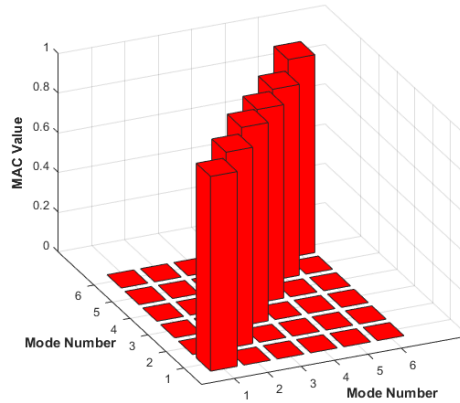


Figure 5.8: 3D MAC plot example.

5.4 Results

In order to demonstrate Multistage Cyclic Symmetry functionality, in the following subsections two examples will be presented: the first (case A) is related with a simple multistage structure, the second (case B) is more realistic and made up of two blisks with 48 and 54 sectors.

Blisks, or Integrally Bladed Rotors (IBR), are turbomachine components comprising both rotor disk and blades. They can be easily made using additive manufacturing or welding together individual blades to a rotor disk. Since blisks consist of a single part instead of disk assembled with individual removable blades, they are lighter and have better efficiency related to air compression in the engine (up to 8%).

5.4.1 Test case A

The following case of study (Figure 5.9) regards two different stages made up of 8 and 11 sectors. Starting from the base sectors, the multistage cyclic symmetry method will be used running a modal analysis with different harmonic indexes. Furthermore, a modal analysis will be also run for 360 full model representing the cyclic expansion of sectors from both stages of multistage case (Figure 5.10). This confront wants to prove the goodness of results reached using Multistage Cyclic Symmetry as well as the advantages linked with used resources: as we aspect, using a complete model leads to a higher execution time and computation costs required.

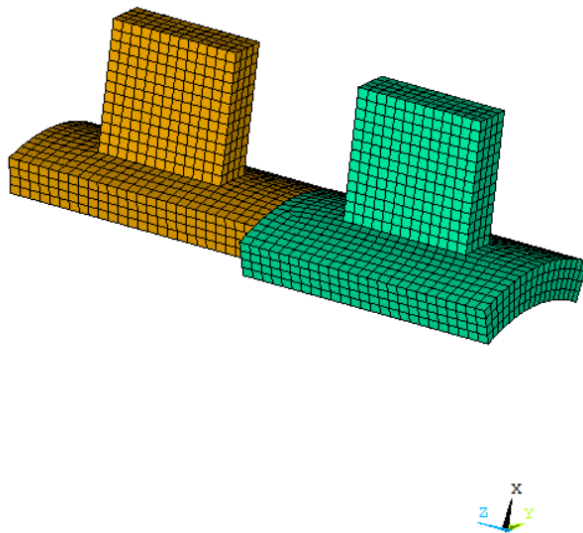


Figure 5.9: Sector from stage 1 (green color) and sector from stage 2 (orange color).

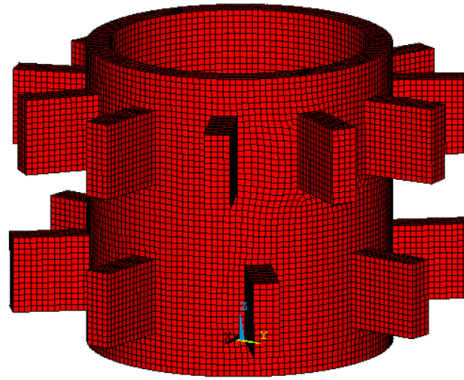


Figure 5.10: 360 full model with two stages of 8 and 11 sectors.

Before presenting results for 360 model, it is important to underline that in this kind of analysis information about Harmonic Index (alias Nodal Diameters) are lost. So that, it is very easy (especially for higher frequencies) confront the wrong 360 model's mode shape with the one from the Multistage model. As an answer to this issue, a best practice can be to diagram displacements of each sectors (from 360 model) and define the "Harmonic Index" referring to the half number of peaks or null displacements. So, in the following example linked with the mode shape shown in Figure 5.11, shelves' nodes are selected from the lower stage (8 sectors) (Figure 5.12) and their displacements along x -, y -, and z -axis are plot in Figure 5.13. The latter figure demonstrates how this mode is related with a Harmonic Index equal to 4.

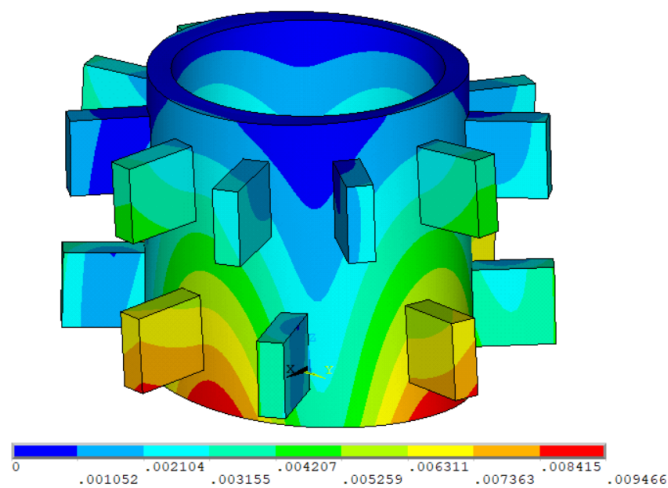


Figure 5.11: Modal shape of 360 full model, Frequency = 71 Hz.

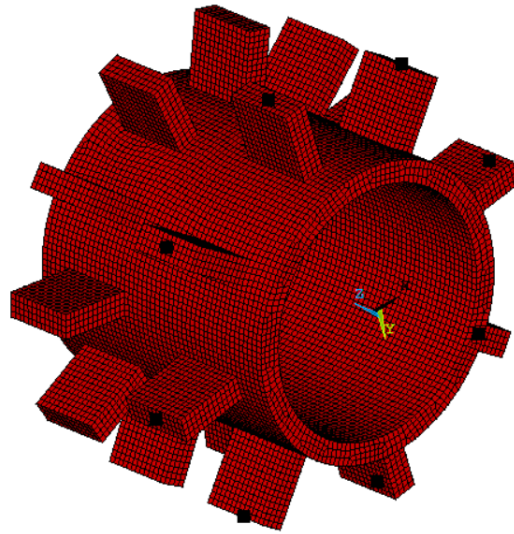


Figure 5.12: nodes selected due to extract Harmonic Index from 360 full model.

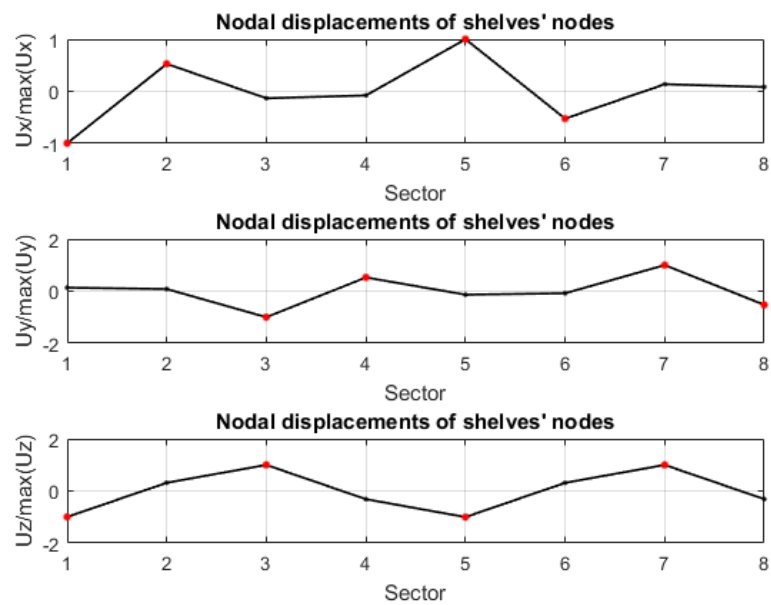


Figure 5.13: Displacements of node selected in Figure 5.12, $Fr = 71$ Hz.

Using this approach for all the modes from a 360 full model, confront with Multistage model can be conducted avoiding errors. In the next pages results of modal analysis for both models are presented.

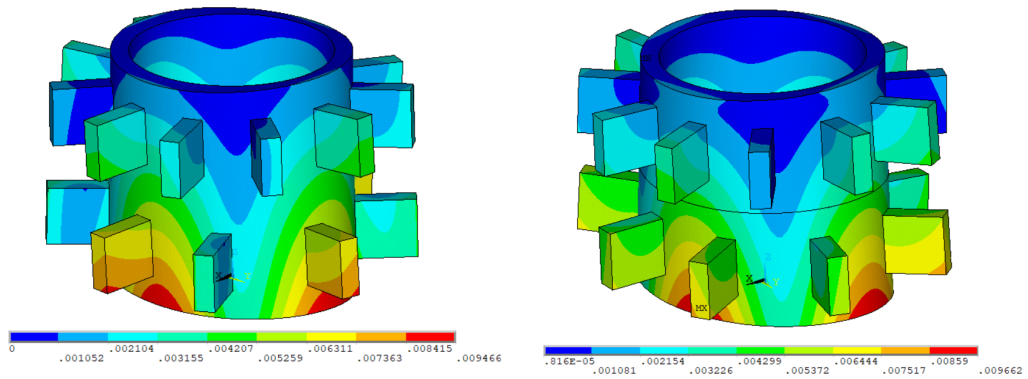


Figure 5.14: Modal shape, Harmonic Index equal to 2 , 360 Model Frequency = 71 Hz (left figure), Multistage Model Frequency = 75 Hz (right figure).

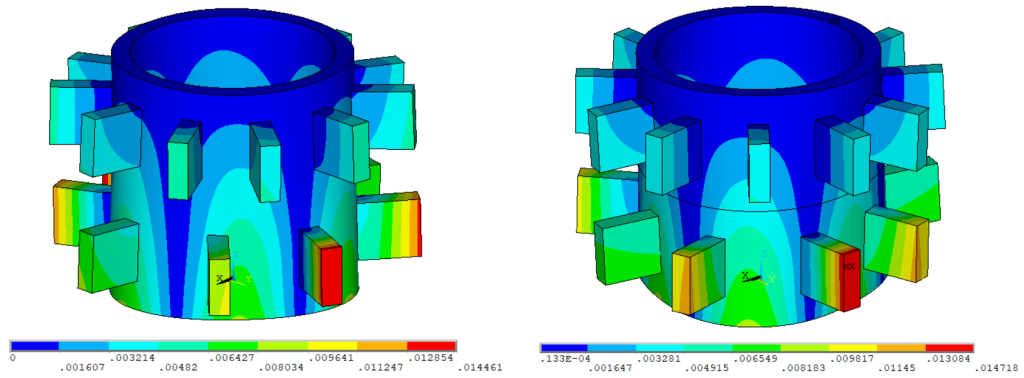


Figure 5.15: Modal shape, Harmonic Index equal to 3 , 360 Model Frequency = 157 Hz (left figure), Multistage Model Frequency = 157 Hz (right figure).

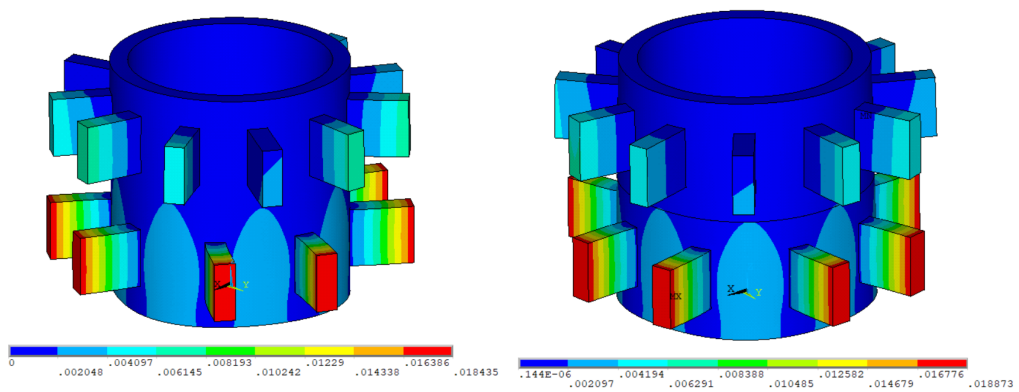


Figure 5.16: Modal shape, Harmonic Index equal to 4 , 360 Model Frequency = 198 Hz (left figure), Multistage Model Frequency = 197 Hz (right figure).

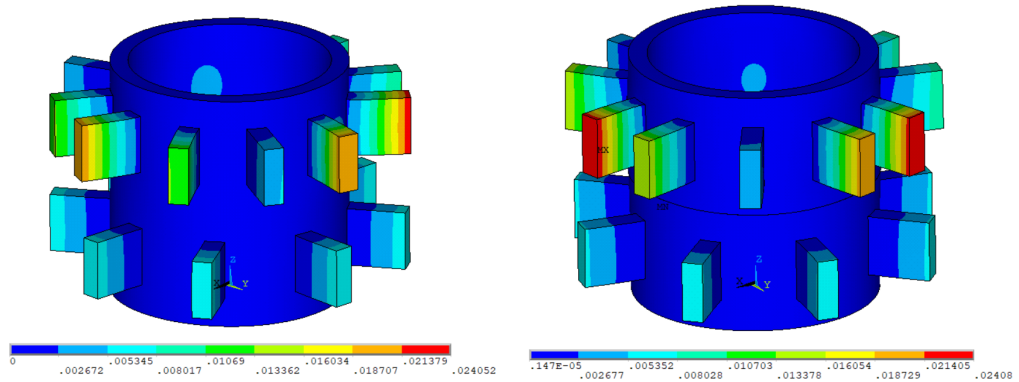


Figure 5.17: Modal shape, Harmonic Index equal to 4 , 360 Model Frequency = 220 Hz (left figure), Multistage Model Frequency = 220 Hz (right figure).

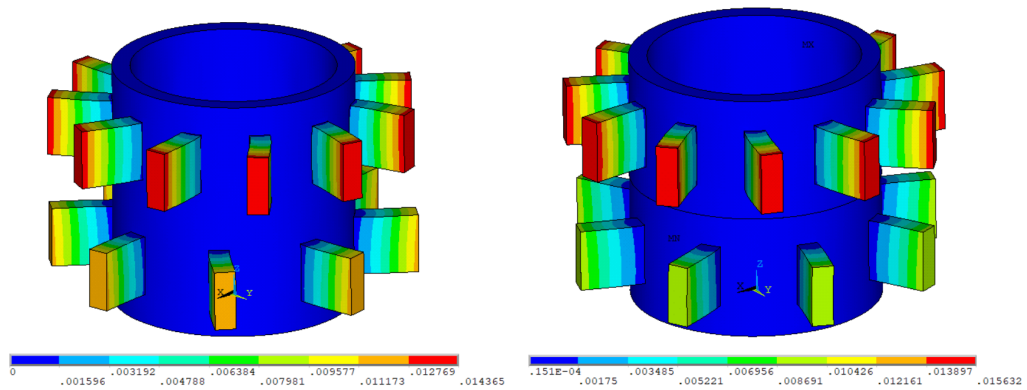


Figure 5.18: Modal shape, Harmonic Index equal to 0 , 360 Model Frequency = 228 Hz (left figure), Multistage Model Frequency = 239 Hz (right figure).

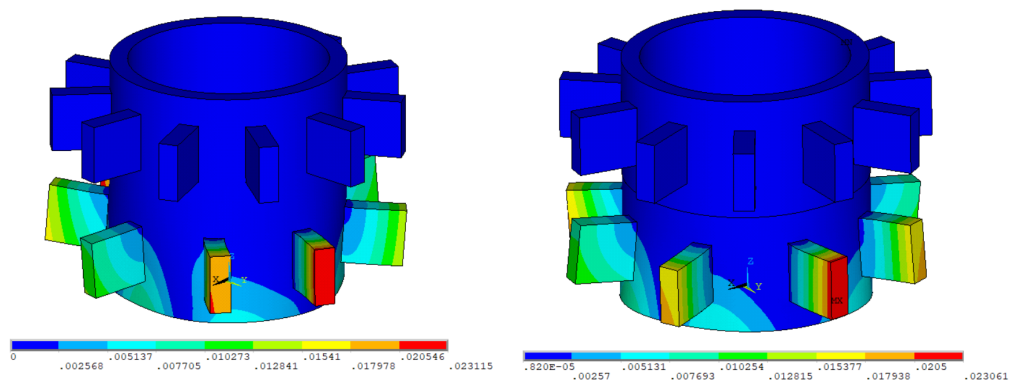


Figure 5.19: Modal shape, Harmonic Index equal to 3 , 360 Model Frequency = 240 Hz (left figure), Multistage Model Frequency = 241 Hz (right figure).

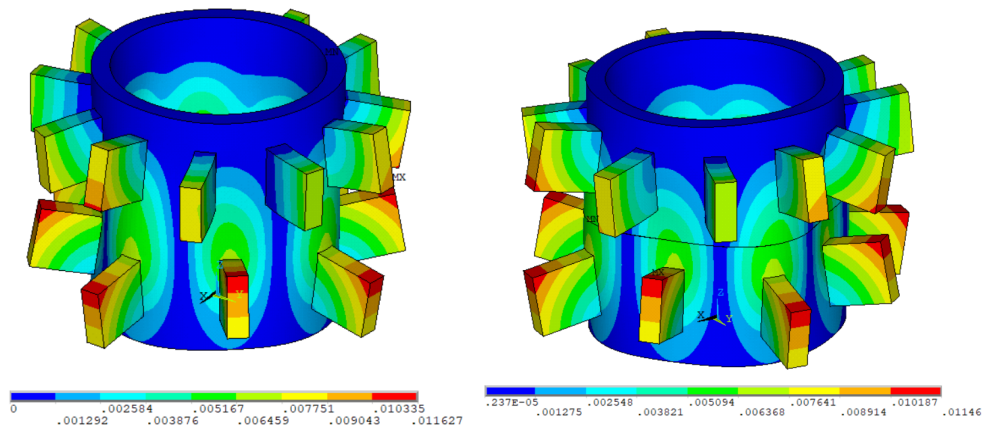


Figure 5.20: Modal shape, Harmonic Index equal to 4 , 360 Model Frequency = 306 Hz (left figure), Multistage Model Frequency = 305 Hz (right figure).

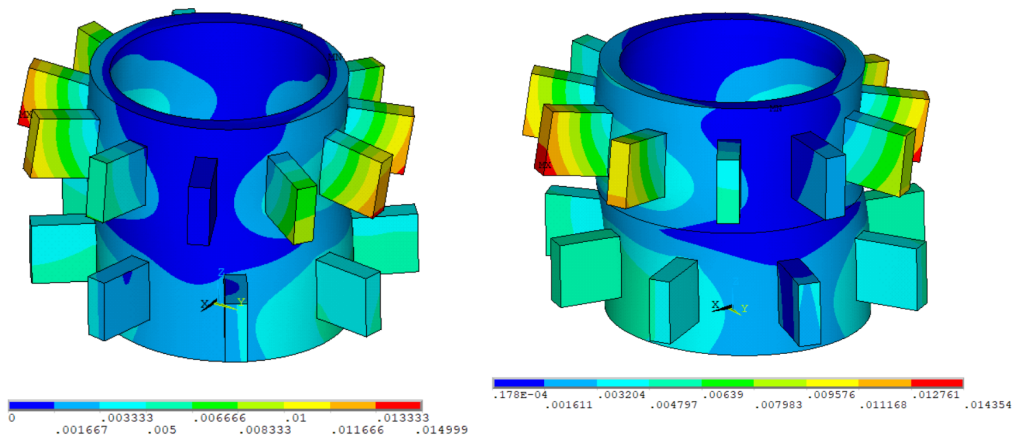


Figure 5.21: Modal shape, Harmonic Index equal to 1 , 360 Model Frequency = 340 Hz (left figure), Multistage Model Frequency = 340 Hz (right figure).

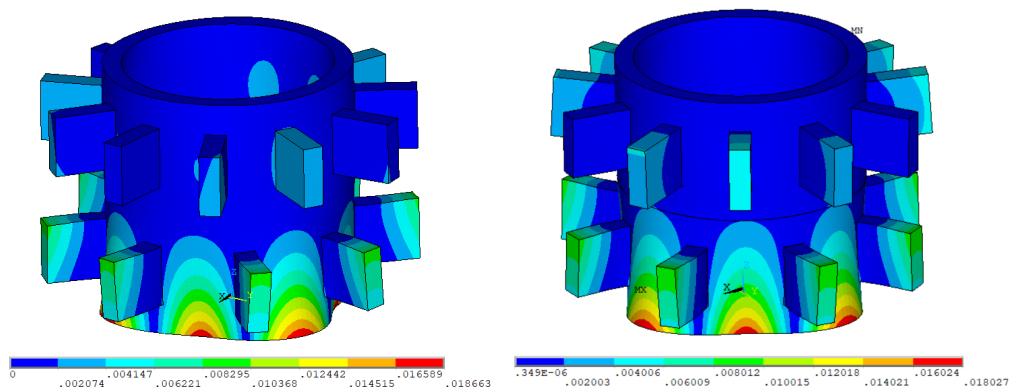


Figure 5.22: Modal shape, Harmonic Index equal to 4 , 360 Model Frequency = 461 Hz (left figure), Multistage Model Frequency = 459 Hz (right figure).

MAC results case A

Pointing out results obtained above, here MAC is computed for the previous analyzed modes due to check their accuracy; results follow below.

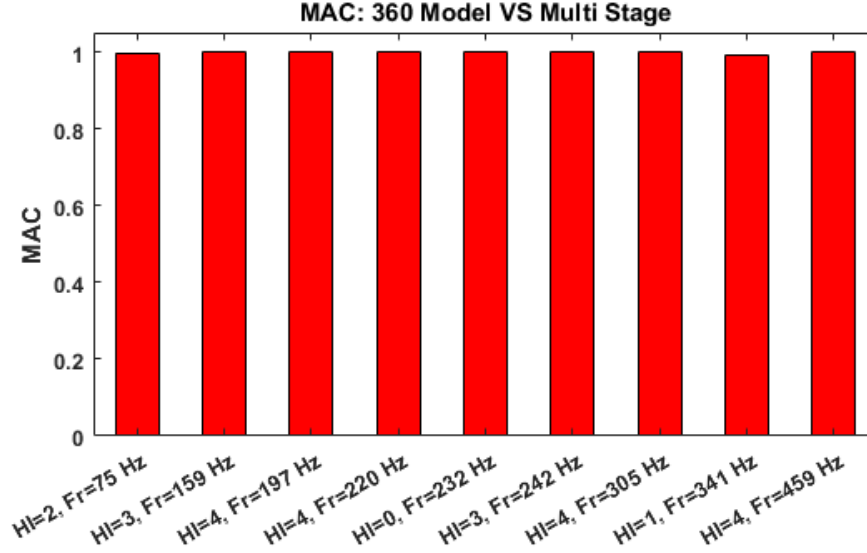


Figure 5.23: MAC calculation: Multistage VS 360 full model (case A).

As image shows, Multistage and 360 full model have consistent mode shapes. Due to clarify MAC results, a table, reporting the obtained MAC values and the difference in terms of frequencies (5.6) from Multistage and 360 model, is attached below (Table 5.1).

$$err = \frac{|Fr_{MS} - Fr_{360}|}{Fr_{MS}} \quad (5.6)$$

Mode	Frequency Error (eq. 5.6)	MAC
Fig. 5.14	5.63 %	0.9973
Fig. 5.15	0.32 %	0.9983
Fig. 5.16	0.51 %	1
Fig. 5.17	0.23 %	1
Fig. 5.18	4.82 %	0.9682
Fig. 5.19	0.42 %	0.9996
Fig. 5.20	0.33 %	1
Fig. 5.21	0.15 %	0.9922
Fig. 5.22	0.43 %	0.9981

Table 5.1: Modal Analysis confront between Multistage and 360 full model (case A).

5.4.2 Test case B

In the following example two blisks are used. The first (the blue one shown in the Figure 5.24) is made up of 48 sectors, the second (the green one) consists of 54. As done in the previous test case, starting from the base sectors, Multistage Cyclic Symmetry will be applied due to obtain modal analysis. Results will be also compared (using MAC computation) with the ones from a 360 full model (Figure 5.25).

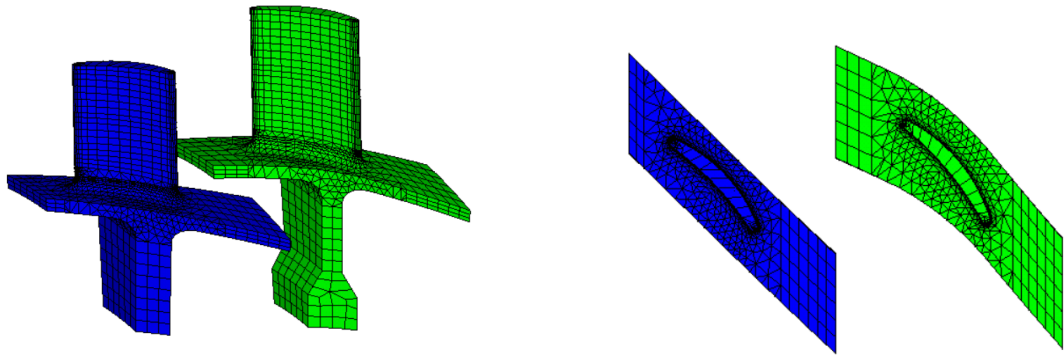


Figure 5.24: Sector from stage 1 (blue color) and sector from stage 2 (green color). Left figure shows isometric view; right one top view.

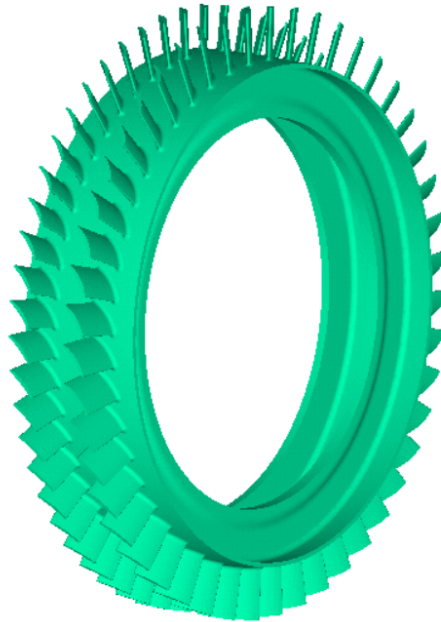


Figure 5.25: 360 full model with two stages of 48 and 54 sectors (mesh has been hid due to obtain a clearer visualization).

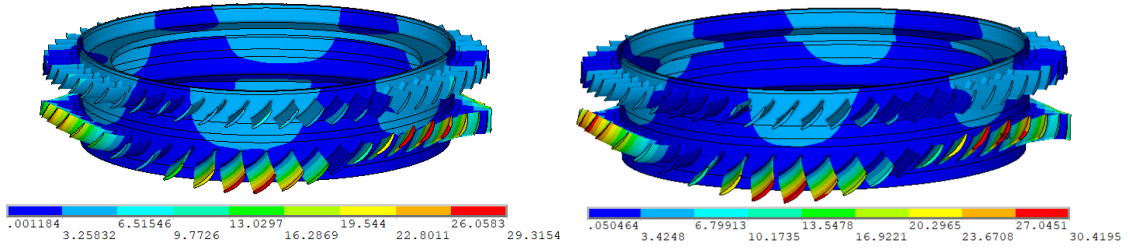


Figure 5.26: Modal shape, Harmonic Index equal to 3 , 360 Model Frequency = 1529 Hz (left figure), Multistage Model Frequency = 1507 Hz (right figure).

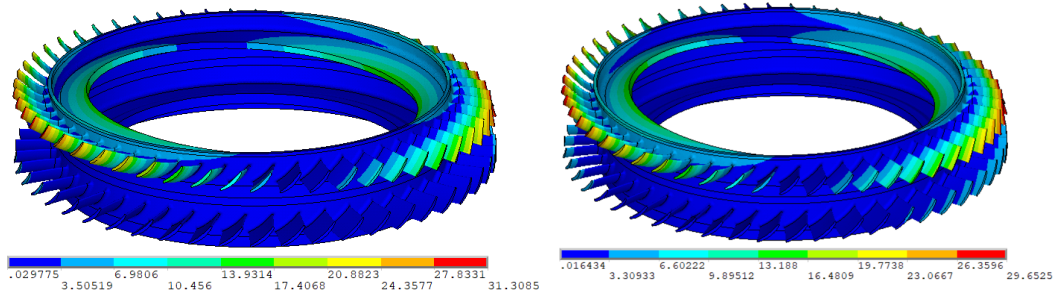


Figure 5.27: Modal shape, Harmonic Index equal to 1 , 360 Model Frequency = 1521 Hz (left figure), Multistage Model Frequency = 1525 Hz (right figure).

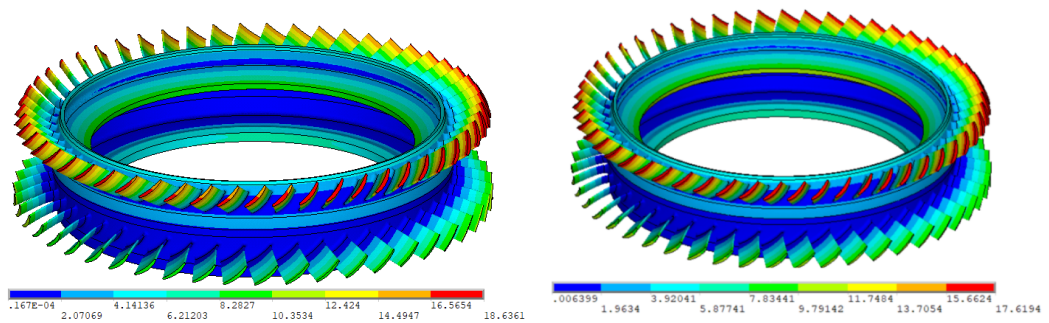


Figure 5.28: Modal shape, Harmonic Index equal to 0 , 360 Model Frequency = 1620 Hz (left figure), Multistage Model Frequency = 1620 Hz (right figure).

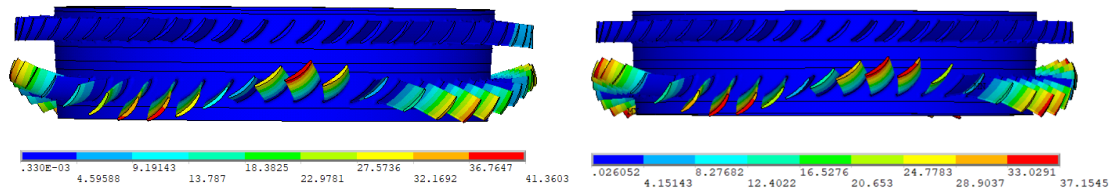


Figure 5.29: Modal shape, Harmonic Index equal to 4 , 360 Model Frequency = 1637 Hz (left figure), Multistage Model Frequency = 1634 Hz (right figure).

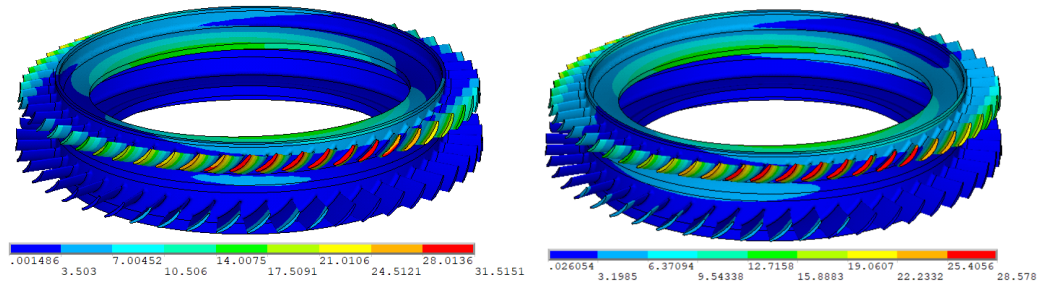


Figure 5.30: Modal shape, Harmonic Index equal to 1 , 360 Model Frequency = 2571 Hz (left figure), Multistage Model Frequency = 2562 Hz (right figure).

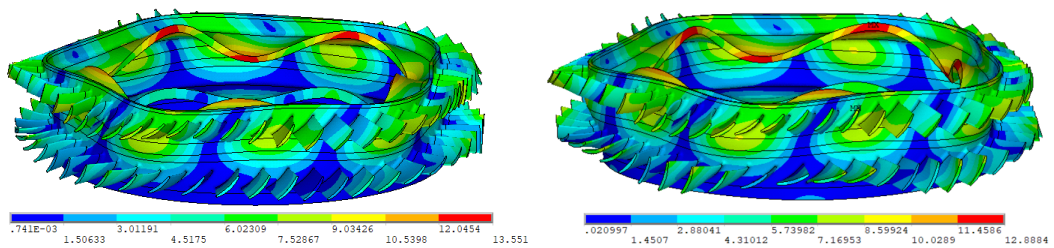


Figure 5.31: Modal shape, Harmonic Index equal to 5 , 360 Model Frequency = 4114 Hz (left figure), Multistage Model Frequency = 4109 Hz (right figure).

MAC results case B

Pointing out results obtained above, here MAC is computed for the previous analyzed modes due to check their accuracy; results follow below. As image shows, Multistage

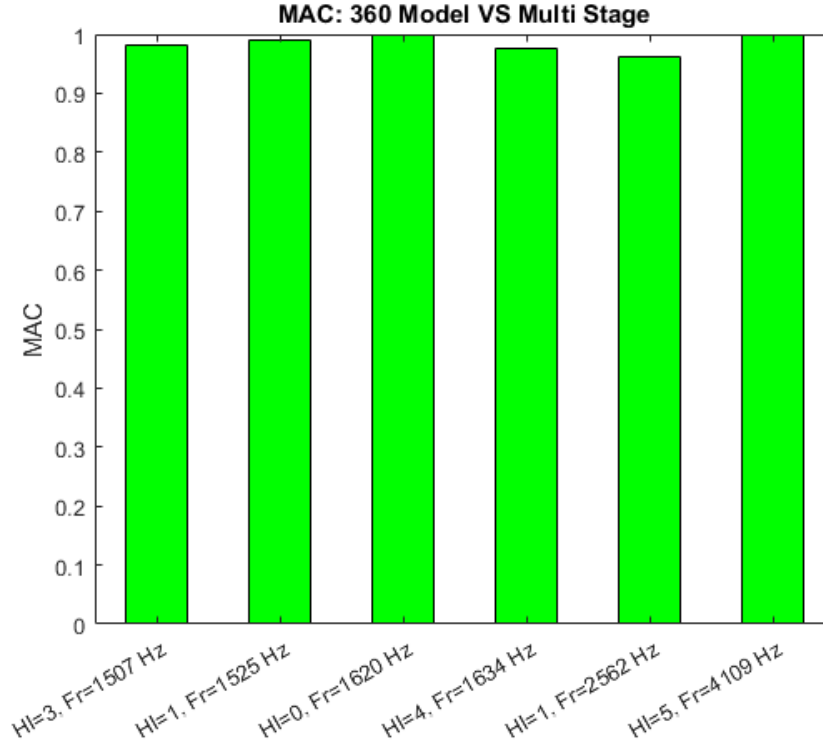


Figure 5.32: MAC calculation: Multistage VS 360 full model (case B).

and 360 full model have consistent mode shapes. Due to clarify MAC results, a table, reporting the obtained MAC values and the difference in terms of frequencies (5.6) from Multistage and 360 model, is attached below (Table 5.2).

Mode	Frequency Error (eq. 5.6)	MAC
Fig. 5.26	1.44 %	0.9873
Fig. 5.27	0.26 %	0.9913
Fig. 5.28	0.03 %	1
Fig. 5.29	0.18 %	0.9646
Fig. 5.30	0.23 %	0.9592
Fig. 5.31	0.19 %	1

Table 5.2: Modal Analysis confront between Multistage and 360 full model (case B).

Chapter 6

Forced Response of Multistage Cyclic Structures

A best practice during the project of a LPT, as bladed disks, is to design this component by avoiding any coincidence of the modal response to the engine excitation. Since, in the previous section, results from modal analysis have been presented, here a confront of harmonic analyses obtainable with a Multistage Cyclic Symmetry and a 360 full model is proposed for both test cases. Additionally, it is also considered the forced response of single stages extracted from the the above-mentioned models.

For the multistage case of study forced response is computed using the "superposition principle" (that sums factored mode shapes obtained from a previous modal analysis) to calculate the harmonic response) following the same procedure adapted in a typical single stage cyclic symmetry analysis. In the following examples nodal diameters, alias harmonic index, are set for both stages with the same value. However, according to Laxalde et al. [14], the dynamics of the multi-stage system can feature simultaneous contributions of different nodal diameters.

In order to excite our system, a traveling wave excitation will be applied:

$$F_z = F_0 e^{i \cdot EO \cdot t_h} \quad , \quad t_h = \{0, d_{th}, 2 \cdot d_{th}, \dots, 2\pi - d_{th}\} \quad , \quad d_{th} = \frac{2\pi}{n_b} \quad , \quad (6.1)$$

with F_0 max excitation's value, n_b number of blades and EO engine order.

Due to understand the advantages of using Multistage Cyclic Symmetry as an useful tool coupled with Single Stage Cyclic Symmetry, forced response will be also computed for single sector in cyclic symmetry. Even if the *commercial fem tool* used in this thesis does not allow harmonic analyses for Multistages, we were able to obtain some results. Since this problem, the 360 full model's results will be our "reference case".

First, a modes comparison between Single Stage, Multistage and 360 Full Model is required. Once we are sure that mode shapes are consistent, these will be excited using a traveling wave excitation (eq. 6.1). Results follow for both test cases.

6.1 Results

As shown below, for each models harmonic analyses are computed for two main cases: the former in which the mode shape is confined only to the single stage (that shares the same boundary conditions of Multistage and 360 full model); the latter in which the coupling effect between the two stages plays an important role. In this last case, analyses show not a good matching in terms of frequency and max amplitude between the three models (360, Multistage, Single Stage).

6.1.1 Test case A

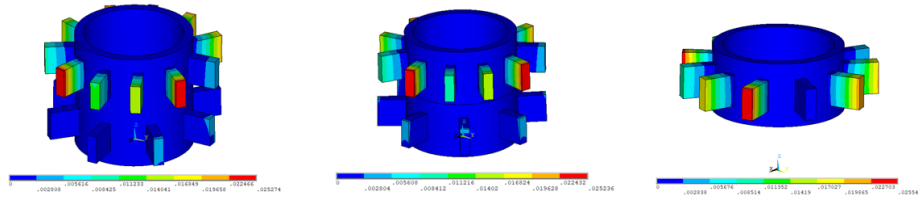


Figure 6.1: 360 Full Model (left) vs Multistage (center) vs Single Stage (right) - Mode 1 - Harmonic Index = 2.

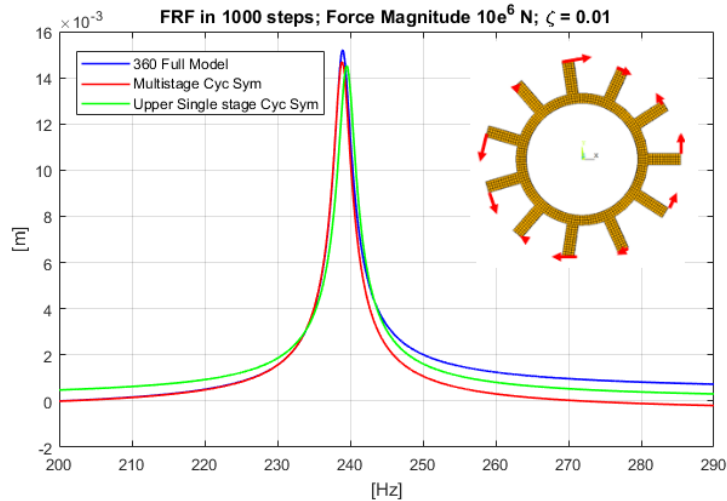


Figure 6.2: Excitation applied on the upper stage. Good matching in terms of Frequency Response in case no coupling effect is shown.

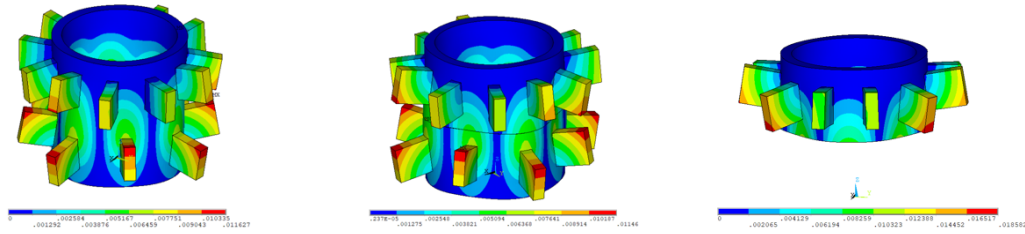


Figure 6.3: 360 Full Model (left) vs Multistage (center) vs Single Stage (right) - Mode 4 - Harmonic Index = 4.

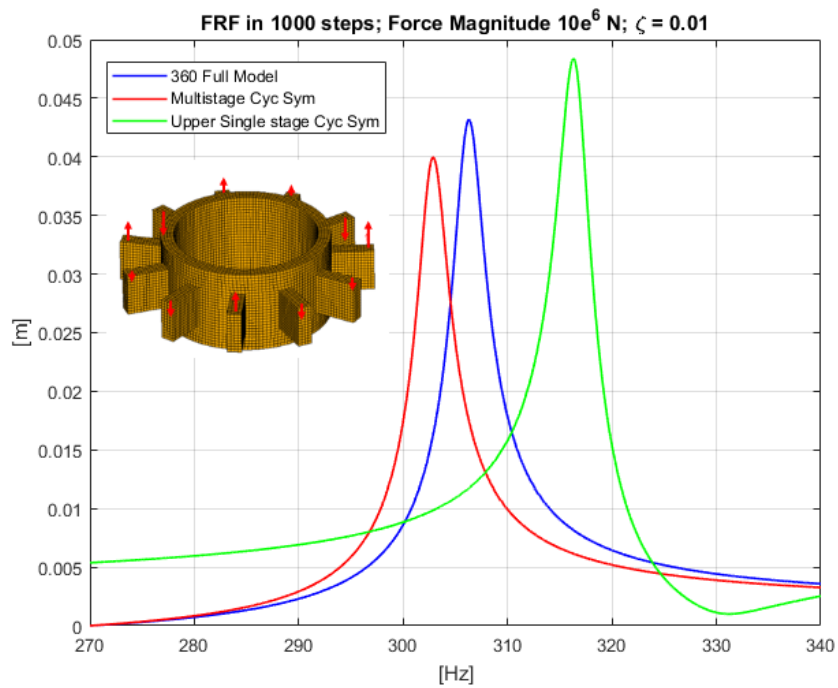


Figure 6.4: Excitation applied on the upper stage. Not good matching in terms of Frequency Response in case coupling effect is significant.

6.1.2 Test case B

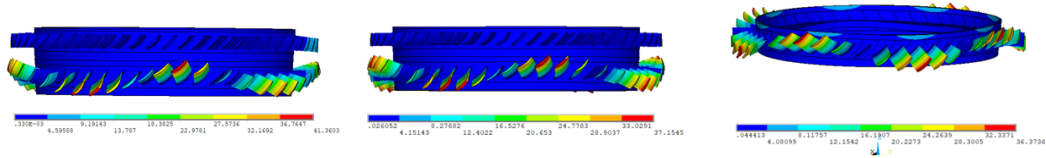


Figure 6.5: 360 Full Model (left) vs Multistage (center) vs Single Lower Stage (right) - Mode 10 - Harmonic Index = 4.

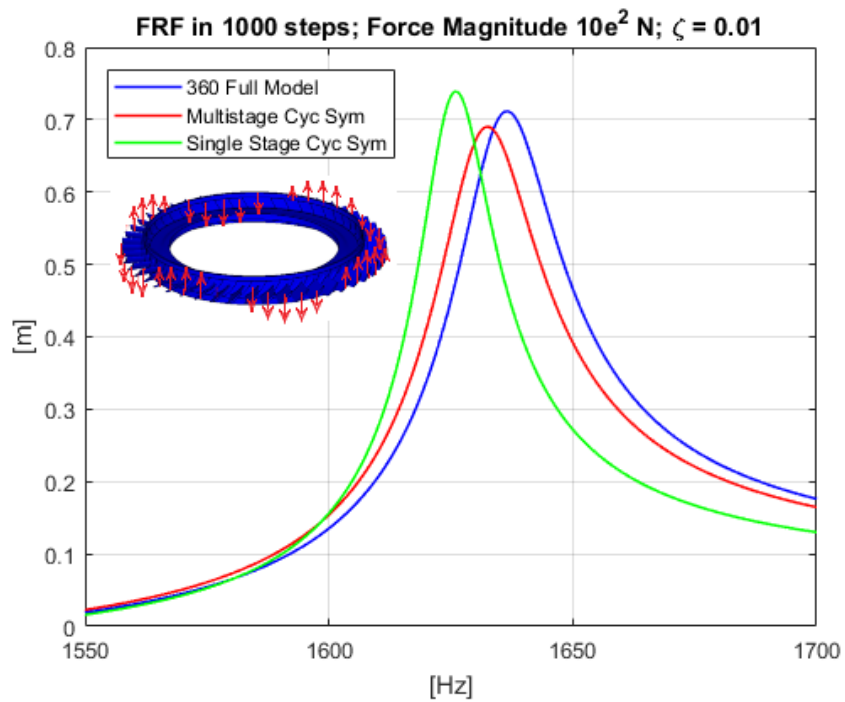


Figure 6.6: Excitation applied on the lower stage. Good matching in terms of Frequency Response in case no coupling effect is shown.

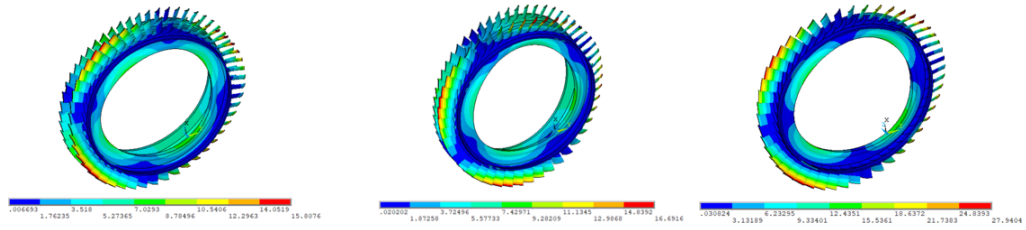


Figure 6.7: 360 Full Model (left) vs Multistage (center) vs Single Lower Stage (right) - Mode 4 - Harmonic Index = 2.

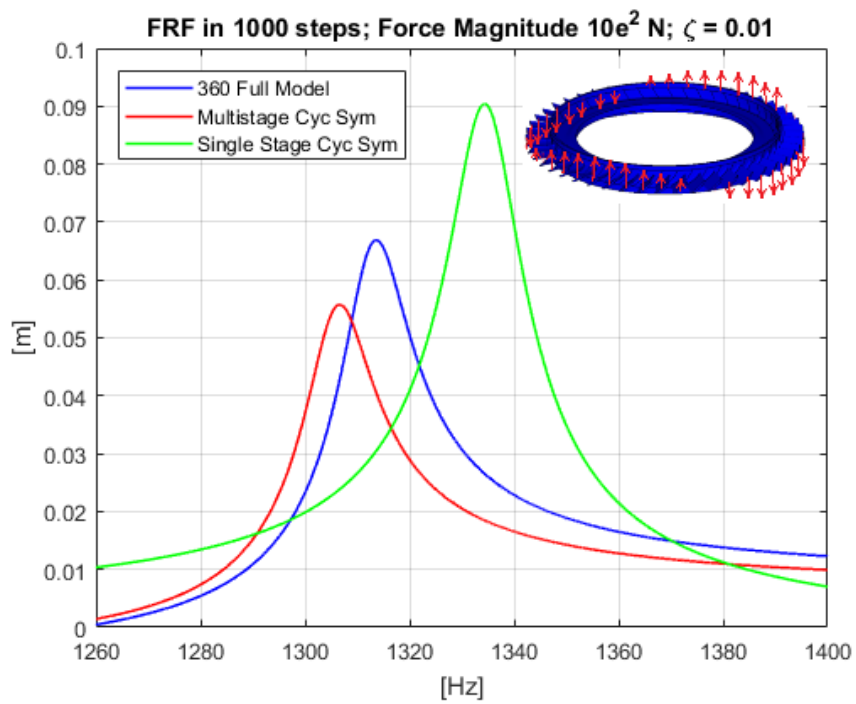


Figure 6.8: Excitation applied on the lower stage. Not good matching in terms of Frequency Response in case coupling effect is significant.

Chapter 7

Conclusions and future developments

Modal Analysis

Multistage cyclic symmetry gives access to the actual shaft geometry. It is based on the cyclic symmetry modeling of individual stages then coupled. This method appears quite simple since coupling is possible even if stages have different interstage mesh.

In this thesis a *commercial fem tool* has been used due to apply cyclic symmetry to multistage structures. So that, modal analysis has been conducted confronting results with the ones from a 360 full model. These confronts, also in terms of MAC calculation, prove that the Multistage Cyclic Symmetry method shows good accuracy with a less lower computational costs compared to the full model. In the present application, complete analysis ran in less than 5 mn, while 360 full models' analysis ran in almost 1 hour.

Forced Response

As written above, a best practice during the project of a LPT, as bladed disks, is to design this component by avoiding any coincidence of the modal response to the engine excitation. So that, in this overview, harmonic analyses can be an useful substep to define the system response to external loads. Even though the *FEM tool* here used does not allow this type of analysis for a Multistage structure using cyclic symmetry, some results (showed in the previous chapter) have been obtained and confronted to a Single stage and a 360 full model. The last confront is necessary in order to be confident with results from Multistage model.

Comparison between results proves how coupling effect plays an important role: both test cases show good matching in terms of Frequency Response in case of mode shape

confined to the single stage, while frequencies and max amplitudes are different for Single Stage and Multistage or 360 when coupling between stages is significant.

So that, Multistage cyclic symmetry method can be an useful tool for all the cases in which interstage coupling cannot be neglected as well as a good approach for a preliminary assessment.

Bibliography

- [1] *Aircraft Turbine Engine*. URL: <https://www.sourcingstreamlined.com/apu-capabilities-parts/>.
- [2] G. Battiato and C.M. Firrone. «A modal based reduction technique for wide loose interfaces and application to a turbine stator». In: *Mechanical Systems and Signal Processing* 139 (2020), p. 106415.
- [3] G. Battiato et al. «Reduction and coupling of substructures via Gram–Schmidt Interface modes». In: *Computer Methods in Applied Mechanics and Engineering* 336 (2018), pp. 187–212.
- [4] Giuseppe Battiato. «Vibrations prediction and measurement of multi-stage bladed disks with non linear behavior due to friction contacts». PhD thesis. Politecnico di Torino, 2017.
- [5] Fabio Bellacicco. *Stabilizzazione di uno stadio di LPT bladed-disk in presenza della condizione di instabilita a flutter mediante mistuning intenzionale*. Master Thesis, Politecnico di Torino, 2016.
- [6] Andrea Bray. «Unsteady fluid-structure interaction in aeronautical low pressure turbines.» PhD thesis. Politecnico di Torino, 2018.
- [7] *Brayton cycle*. URL: <https://en.wikipedia.org/wiki/Friction>.
- [8] Pierre C. «Mode Localization and Eigenvalue Loci Veering Phenomena in Disordered Structures». In: *Journal of Sound and Vibration* 126 (1988), pp. 485–502.
- [9] *Cholesky decomposition*. URL: https://en.wikipedia.org/wiki/Cholesky_decomposition.
- [10] Giancarlo Genta. *Vibration dynamics and control*. Vol. 616. Springer, 2009.
- [11] James Gere and Barry Goodno. «Mechanics of materials». In: (2009).
- [12] *Great 2020*. URL: <https://www.great2020.it>.
- [13] Dewey H. Hodges and G. Alvin Pierce. *Introduction to structural dynamics and aeroelasticity*. Vol. 15. Cambridge University Press, 2011.

- [14] Denis Laxalde, Jean-Pierre Lombard, and Fabrice Thouverez. «Dynamics of Multistage Bladed Disks Systems». In: *Journal of Engineering for Gas Turbines and Power* 4.129 (2007), pp. 1058–1064.
- [15] *LU decomposition*. URL: https://en.wikipedia.org/wiki/LU_decomposition.
- [16] Lassalle M. «Self-excited vibrations controlled by damping at blade root joints of turbine disks». PhD thesis. Politecnico di Torino, 2018.
- [17] Paolo Maggiore, Marco Moletta, and Alberto Civardi. «Development and Validation of Algorithms for Vibration Monitoring of Aeronautical Engines». In: (2019).
- [18] Ansys® Mechanical. «Multistage Cyclic Symmetry Analysis Guide». In: *ANSYS, Inc.* (Version 2021 R2).
- [19] Miroslav Pastor, Michal Binda, and Tomáš Harčarik. «Modal Assurance Criterion». In: *Procedia Engineering* 48 (2012), pp. 543–548.
- [20] Valeria Pinto. «Aeromechanical Optimization of Aeronautical Low Pressure Turbine Components». PhD thesis. Politecnico di Torino, 2020.
- [21] Amedeo Ramieri. «Analisi e comparazione di diversi modelli di contatto all'interlocking per rotori di turbine di bassa pressione». In: *Politecnico di Torino–2017* (2017).
- [22] Rolls-Royce. *The Jet Engine*. 1996.
- [23] A.V. Srinivasan. «Flutter and resonant vibration characteristics of engine blades». In: (1997).
- [24] D. L. Thomas. «Dynamics of rotationally periodic disks assemblies - a selected survey». In: *International Journal for Numerical Methods in Engineering* 14 (1979), pp. 81–102.
- [25] *Turbofan*. URL: <https://en.wikipedia.org/wiki/Turbofan>.
- [26] *Turbojet*. URL: <https://en.wikipedia.org/wiki/Turbojet>.
- [27] *Turboprop*. URL: <https://en.wikipedia.org/wiki/Turboprop>.
- [28] *Turboshaft*. URL: <https://en.wikipedia.org/wiki/Turboshaft>.
- [29] *Wake*. URL: <https://en.wikipedia.org/wiki/Wake>.